

How does air-sea wave interaction affect tropical cyclone intensity? An atmosphere-wave-ocean coupled model study based on super typhoon Mangkhut (2018)

Zhenning Li¹, Chi-Yung Francis Tam², Yubin Li³, Gabriel Lau², Junwen Chen⁴, S.T. Chan⁵, Dick-Shum Dickson Lau⁵, and Yiyi Huang⁶

¹Institute of Environment, Energy and Sustainability, The Chinese University of Hong Kong

²Chinese University of Hong Kong

³Nanjing University of Information Science and Technology

⁴Shenzhen Wiselec Technology Co., Ltd.,

⁵Hong Kong Observatory

⁶Department of Hydrology and Atmospheric Sciences, University of Arizona

November 21, 2022

Abstract

Capturing TC intensity change remains a great challenge for most state-of-the-art operational forecasting systems. Recent studies found the TC intensity forecasts are sensitive to three-dimensional ocean dynamics and air-sea interface processes beneath extreme winds. By performing a series of numerical simulations based on hierarchical Atmosphere–Wave–Ocean (AWO) coupling configurations, we showed how atmosphere-ocean and atmosphere-sea wave coupling can affect the intensity of super typhoon Mangkhut (2018). The AWO coupled model can simulate TC-related strong winds, oceanic cold wake, and wind waves with high fidelity. With atmosphere-ocean (AO) coupling implemented, the simulated maximum surface wind speed is reduced by 7 m/s compared to the atmosphere-only run, due to TC-induced oceanic cold wakes in the former experiment. In the fully coupled AWO simulations, the wind speed deficit can be completely compensated by the wave-air coupling effect. Further analyses showed that, in the AWO experiment, two mechanisms contribute to the improvement of TC intensity. First, in the high wind scenario (>28m/s), the surface drag coefficient reaches an asymptotic level, assisting extreme wind speed to be maintained within the eyewall. Second, the wind speed distribution is modulated and becomes broader; higher wind within the TC area helps to offset the negative effect due to leveling off of the heat exchange coefficient as wind speed increases. Overall, the simulated TC in the AWO run can extract 8-9% more total heat energy from the ocean to maintain its strength, compared to that from the AO experiment.

Hosted file

essoar.10508846.1.docx available at <https://authorea.com/users/531426/articles/597643-how-does-air-sea-wave-interaction-affect-tropical-cyclone-intensity-an-atmosphere-wave-ocean-coupled-model-study-based-on-super-typhoon-mangkhut-2018>

**How does air-sea wave interaction affect tropical cyclone intensity?
An atmosphere–wave–ocean coupled model study based on super typhoon Mangkhut (2018)**

Zhenning Li¹, Chi-Yung Tam^{1,2}, Yubin Li⁴, Ngar-Cheung Lau^{1,3}, Junwen Chen⁵, S.T. Chan⁶, Dick-Shum Dickson Lau⁶ and Yiyi Huang⁷

¹ *Institute of Environment, Energy and Sustainability, The Chinese University of Hong Kong, Hong Kong, China*

² *Earth System Science Programme, The Chinese University of Hong Kong, Hong Kong, China*

³ *Department of Geography Resource Management, The Chinese University of Hong Kong, Hong Kong, China*

⁴ *School of Atmospheric Physics, Nanjing University of Information Science & Technology, Nanjing, China*

⁵ *Shenzhen Wiselec Technology Co., Ltd., Shenzhen, Guangdong, China*

⁶ *Hong Kong Observatory, Hong Kong, China*

⁷ *Department of Hydrology and Atmospheric Sciences, University of Arizona, Tucson, USA*

Submitted to *Earth and Space Science*

Nov 2021

*Corresponding author: Dr. Chi-Yung Francis Tam, Earth System Science Programme, the Chinese University of Hong Kong (E-mail: Francis.tam@cuhk.edu.hk)

Key Points:

- Regional Atmosphere–Wave–Ocean (AWO) coupled models have been customized to study the super typhoon Mangkhut (2018).
- atmosphere-ocean (AO) coupling reduces TC’s surface maximum wind, but AWO simulation can completely compensate that deficit.
- Surface drag coefficient leveling off and broader wind speed distribution function helps to maintain the TC intensity.

Abstract

Capturing TC intensity change remains a great challenge for most state-of-the-art operational forecasting systems. Recent studies found the TC intensity forecasts are sensitive to three-dimensional ocean dynamics and air-sea interface processes beneath extreme winds. By performing a series of numerical simulations based on hierarchical Atmosphere–Wave–Ocean (AWO) coupling configurations, we showed how atmosphere-ocean and atmosphere-sea wave coupling can affect the intensity of super typhoon Mangkhut (2018). The AWO coupled model can

simulate TC-related strong winds, oceanic cold wake, and wind waves with high fidelity. With atmosphere-ocean (AO) coupling implemented, the simulated maximum surface wind speed is reduced by 7 m/s compared to the atmosphere-only run, due to TC-induced oceanic cold wakes in the former experiment. In the fully coupled AWO simulations, the wind speed deficit can be completely compensated by the wave-air coupling effect. Further analyses showed that, in the AWO experiment, two mechanisms contribute to the improvement of TC intensity. First, in the high wind scenario ($>28\text{m/s}$), the surface drag coefficient reaches an asymptotic level, assisting extreme wind speed to be maintained within the eyewall. Second, the wind speed distribution is modulated and becomes broader; higher wind within the TC area helps to offset the negative effect due to leveling off of the heat exchange coefficient as wind speed increases. Overall, the simulated TC in the AWO run can extract 8-9% more total heat energy from the ocean to maintain its strength, compared to that from the AO experiment.

Keywords: Tropical cyclone, Air-Wave-Ocean interaction, Surface friction, Structural improvement, Momentum and heat exchange

Introduction

Bringing high sea waves, storm surges, strong winds, torrential rainstorms, and landslides, tropical cyclones (TCs) are one of the most hazardous natural disasters to coastal zones over the world (Emanuel 2005; Klotzbach 2006; Bhatia 2019; Wang et al., 2019). Globally, TCs were the one of the most impactful natural disasters in terms of fatalities, killing 233,000 people between 1998-2017 (Wallemacq et al. 2018). TCs can also cause enormous damages in local economy and environment (e.g., Schmidt et al. 2010; Hoque et al. 2016). Specially, the Guangdong-Hong Kong-Macao Greater Bay Area (hereinafter GD-HK-MO GBA, or simply GBA), with marked increase in its economic strength in recent years, is affected by a dozen of TCs annually, causing billions of dollars of economic losses and hundreds of casualties (Xu et al. 2017; Chen et al. 2020). Reliable TC intensity and track forecasts are crucial for disaster prevention and mitigation of hazards. Indeed, TC track prediction by global models has gradually improved in the last one to two decades (Bender et al. 2007; Roy and Kovordányi 2012; Yamaguchi et al. 2017); however, prediction of TC intensity still needs to be improved (Davis et al. 2008; Judt et al. 2016; Emanuel and Zhang 2016). Even using state-of-the-art high-resolution atmospheric models, some storms still exhibit elusive “rapid intensification” leading to the model underestimation, or in some cases over-intensified in their development (Davis et al. 2008; Murakami et al. 2015; Magnusson et al. 2019).

The scientific community has increasingly recognized that TC evolution depends on the ocean state and various air-sea interface exchange processes. This is especially the case for storm intensity forecasts, which can be sensitive to three-dimensional ocean dynamics and air-sea interactions beneath extreme winds (Chen et al. 2007; Mogensen et al. 2017; Bruneau et al. 2018). One of the well-known TC-ocean interaction phenomena is TC “cold wake”, marked by intense

sea surface cooling of about 1 to 6 °C, due to turbulence mixing by wind stress and Ekman pumping (Shen and Ginis 2003; Janssen 2004; Yablonsky and Ginis 2009; Zhao and Chan 2017). The strength of these cold wakes, depending on the upper-ocean heat content and TC strength, has a strong control on TC intensification (Lloyd and Vecchi 2011; Ito et al. 2015; Mogensen et al. 2017). Note that only by employing interactive ocean circulation models can these important processes be resolved (Yablonsky and Ginis 2009). Meanwhile, sea waves can influence TC dynamics by changing the sea surface friction, which in turn determines the heat and momentum exchange coefficients (Moon et al. 2004; Chen et al. 2013). Powell et al. (2003) analyzed 300 Global Positioning System dropsondes in 15 TCs and found that momentum exchange coefficient can be saturated (or even reduced) at very high surface wind speeds. Observational and laboratory studies confirmed that the roughness length over the ocean tends to plateau at the wind speed of ~30 m/s or higher. This might be related to airflow separation caused by slowly propagating high waves (found over “young sea state”) or lubricating effect due to sea spray (Reul et al. 1999; Powell et al. 2003; Emanuel 2003; Li et al. 2021). Consequently, TC intensity can be sensitive to the sea-state-dependent air-sea interaction. Numerical studies with such effect can achieve more realistic TC structures, compared with atmosphere-only or even atmosphere-ocean coupled models (Davis et al. 2008; Chen et al. 2013). Operational centers such as the European Centre for Medium Range Weather Forecasts (ECMWF) are now using Atmosphere-Wave-Ocean (AWO) coupled models for routine global meteorological and sea state predictions (Magnusson et al. 2019). However, these models have typical spatial resolutions of ~10 km; cumulus convection thus must be parameterized, although TC physics is known to be best captured by models integrated at convection-permitting scales (i.e., 4 km or less; see Zhang et al. 2011). Moreover, these relatively coarse-resolution products from global models cannot meet regional needs for high-definition coastal risk assessment and management, which are essential for timely actions and effective mitigation strategies to reduce TC-related risks.

The above indicates that mechanisms of AWO coupling need to be incorporated for better simulations of TCs by regional models. In this study, we conducted a series of numerical simulations with various degrees of coupling using a AWO coupled modeling system, focusing on a typhoon case. The case considered is Super Typhoon Mangkhut, which was characterized by its extensive circulation, ferocious winds and rapid movement. It caused widespread and serious impacts in Guam, the Philippines, and brought destructive winds and record-breaking storm surges to GBA.

For the rest of this article, section 2 introduces the coupled model system, experimental design to investigate the coupling effect and observational data sets. Section 3 demonstrates the simulation basics and verification of the coupled model. In section 4, the compensating effects of AWO coupling on TC wind are identified. Section 5 further investigates the mechanisms of such compensating effects. In section 6, we summarize the whole article and discuss limitations and further work.

2.1 The Coupled Ocean–Atmosphere–Wave–Sediment Transport (COAWST) modeling system

The COAWST modeling system is an agglomeration of open-source modeling components that has been tailored to investigate coupled processes of the atmosphere, ocean, and waves in the coastal ocean. The COAWST modeling system has been widely used since its development by the United States Geological Survey in 2010 (Warner et al. 2010). Several Atlantic TCs such as Ivan (2004), Ida (2009), and Sandy (2012) that caused huge impacts to North America were studied using COAWST (Olabarrieta et al. 2012; Zambon et al. 2014a; Zambon et al. 2014b). COAWST version 3.6 is used here to investigate the AWO coupling effects. It consists of the following modules: (1) the atmospheric component which is Weather Research and Forecasting Model (WRFv4.1.2), (2) the oceanic component which is Regional Ocean Modeling System (ROMS) 3.7 svn 981, (3) sea wave component which is Simulating WAVes Nearshore (SWAN) v 41.31, and finally (4) the coupler which is Model Coupling Toolkit (MCT) v 2.6.0.

WRF has been extensively used in operational forecasts and academic research and provides a wide range of meteorological applications across scales from tens of meters to thousands of kilometers. The Advanced Research WRF dynamic core solves fully compressible and non-hydrostatic equations allowing one-way or two-way nesting, and with a moving nest to attain high resolution in the domain of interests. ROMS v3.7 is a free-surface, terrain-following, primitive equations ocean model widely used in the scientific community for a variety of applications (e.g., Wilkin et al., 2005). ROMS can be configured to use several advection schemes, turbulence schemes, surface, and bottom boundary layer schemes; it includes several models for bio-optical, sediment, and sea ice applications. Finally, SWAN v41.31 is a third-generation wave model, based on wave action balance equation with sources and sinks. SWAN is known to be able to capture wind-wave generation and propagation in coastal waters; its wave physical schemes can be turned on/off, including refraction, diffraction, shoaling, and wave-wave interactions. Whitecapping, bottom-induced wave breaking, and bottom friction are also included to represent wave dissipation. The above three components are coupled by the MCT coupler, enabling models to exchange state variables in a fully parallelized computing environment. The message passing between different model components by MCT is shown in Figure 1.

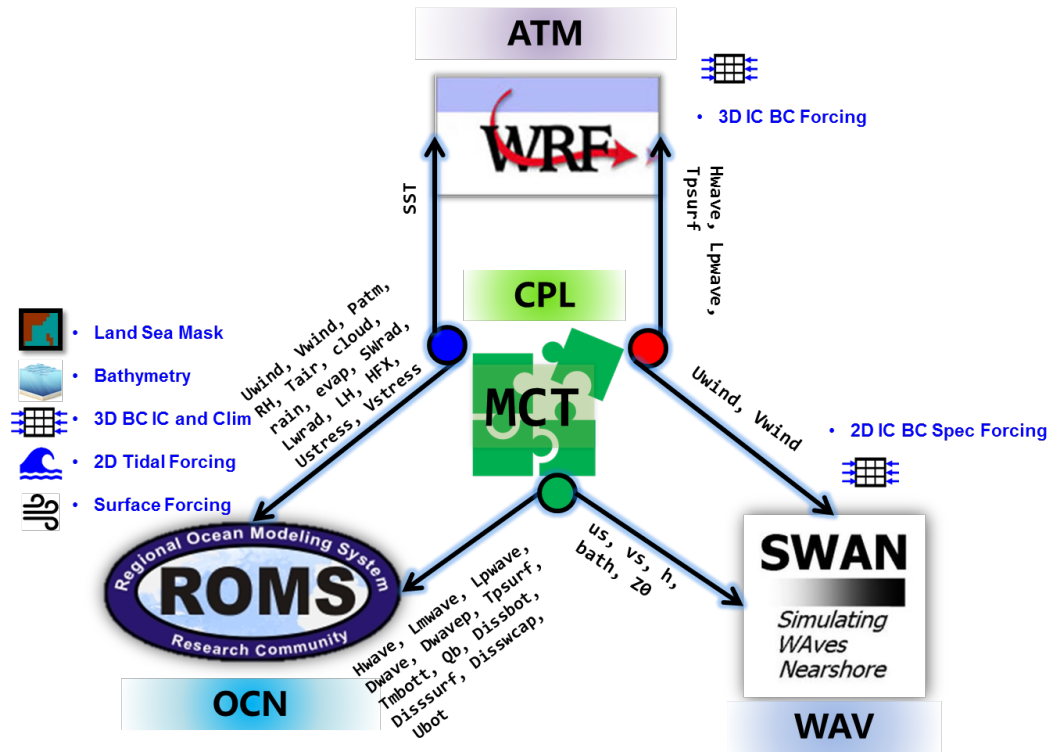


Figure 1 Schematic diagram of the COAWST coupling framework used in this study. The input data and exchanged variables by the Model Coupling Toolkit (MCT) between each component are also summarized.

2.2 Model configurations and experimental design

Super typhoon Mangkhut (2018) was an extremely intense TC in the western North Pacific. After landfall on Luzon at 18:00 UTC on September 14, the mountains of Luzon weakened Mangkhut before it emerged over the South China Sea (SCS) on September 15. Mangkhut continued to move northwestward quickly across the northern part of SCS toward the coast of Guangdong. The storm made landfall again on the Taishan coast of Jiangmen, Guangdong, China, at 09 UTC on September 16, with 10-minute sustained winds of 43 m/s according to Hong Kong Observatory (HKO) best track data. This study focuses on its evolution over northern SCS after its first intense landfall over Luzon. Model domain configurations are specifically set to cover northern SCS and GBA (see Figure 2). The WRF model is integrated at the horizontal resolution of $9 \text{ km} \times 9 \text{ km}$ in its outermost domain (WRF D01), covering part of East to Southeast Asia, SCS and extending into the tropical western Pacific. The domain for ROMS and SWAN (ROMS+SWAN D01) resides within WRF D01,

at the resolution of $2.2 \text{ km} \times 2.2 \text{ km}$ which is eddy-resolving. (This is so even in continental shelf seas where Rossby radius of deformation is much shorter due to shallow bathymetry.) ROMS+SWAN D01 uses open conditions at the northern, eastern and southern boundaries, and closed boundary conditions at the western boundary. The inner domain for WRF (WRF D02) is embedded in ROMS+SWAN D01 at sea, by which it can avoid the discontinuity shock from the uncoupled prescribed sea surface conditions to coupled ocean conditions. Within WRF D02 the convection-permitting resolution of $3 \text{ km} \times 3 \text{ km}$ is adopted. Finer resolution for ROMS+SWAN D01 is constructed compared with that for WRF D02 for several reasons: Firstly, due to simpler physical parameterizations, ROMS and SWAN are relatively lightweight in computation compared with WRF. Secondly, at a $2.2 \text{ km} \times 2.2 \text{ km}$ resolution, not only can ROMS resolve near-shore eddies, but it can also capture wind-driven leeward upwelling and offshore currents, especially for archipelago areas. Finally, the fine-scale ocean surface can better represent surface heterogeneities in extreme weather conditions, which provides more realistic bottom boundary conditions to WRF.

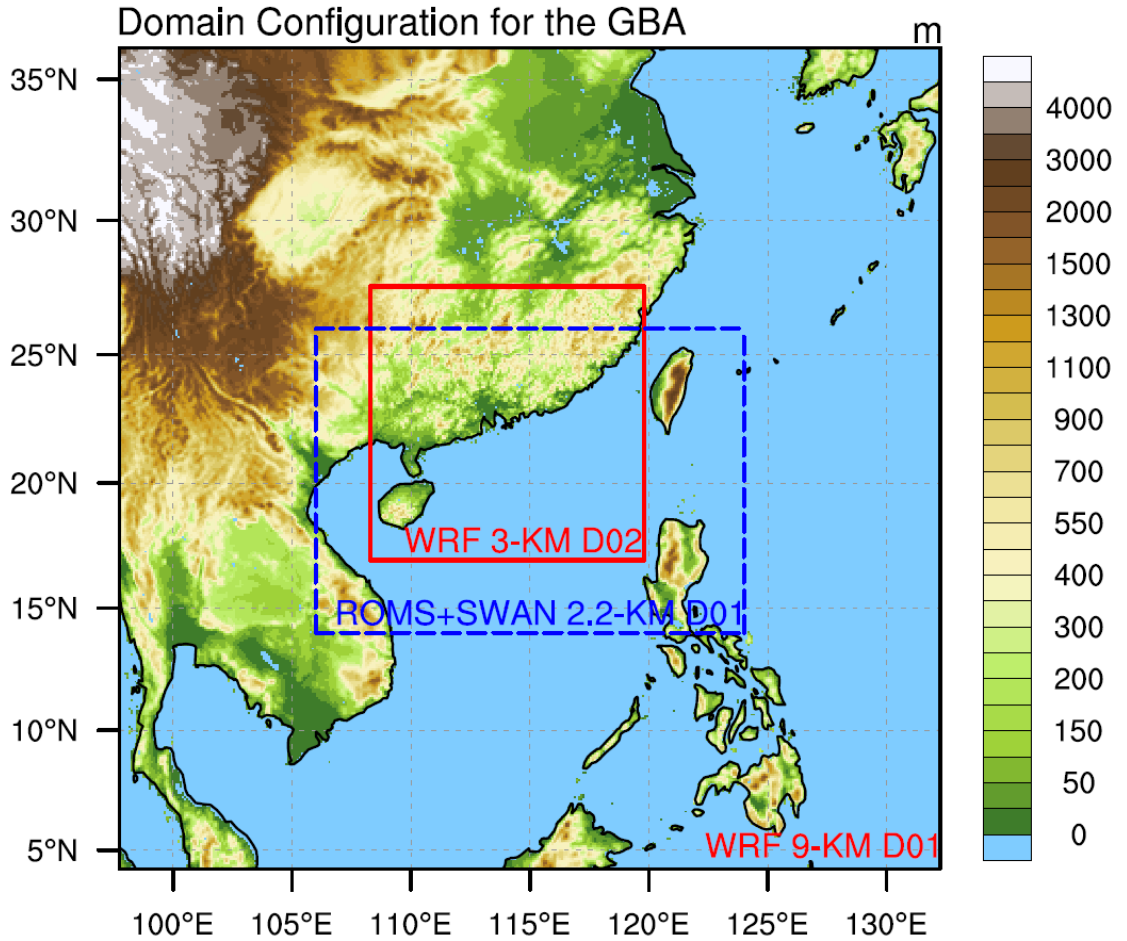
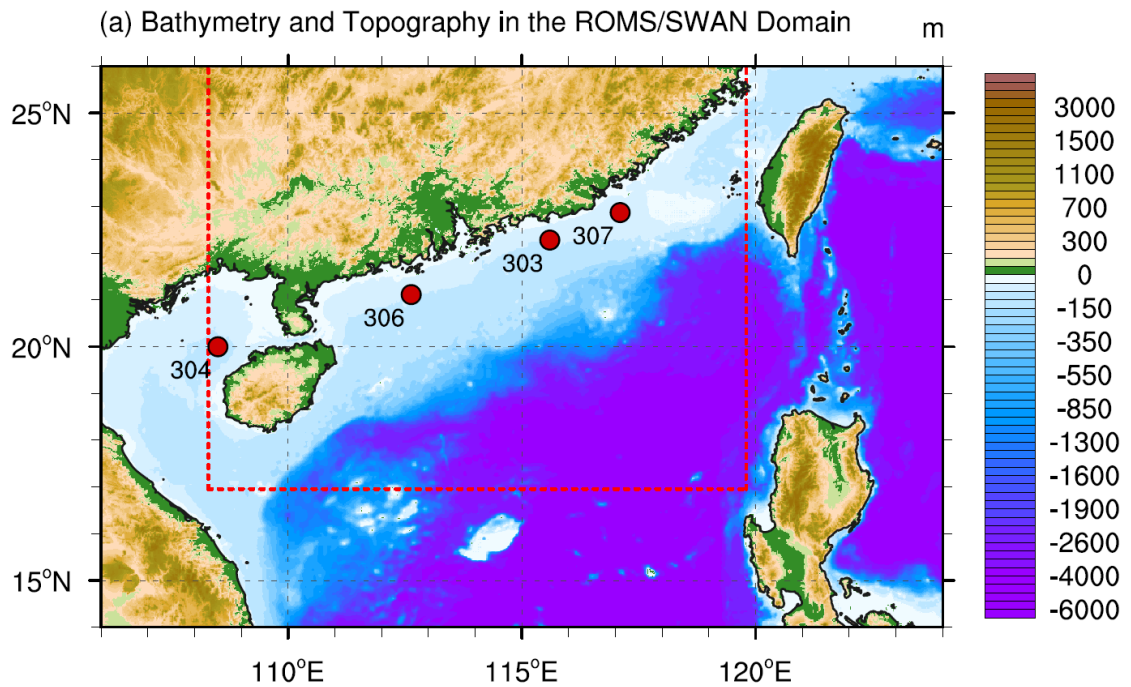


Figure 2 WRF/ROMS/SWAN domain configurations over the GBA. The outermost domain is 9-km WRF D01, and the red box represents the boundary of 3-km WRF D02. The blue dashed box denotes the 2.2-km ROMS/SWAN domain. Shading gives the terrain height within 9-km WRF D01.

Meticulous bathymetry pre-processing is the key procedure for smooth ROMS integration. Original bathymetry in ROMS+SWAN D01 is shown in Fig. 3a. Bounded in the north by coastline of South China, SCS is only hundreds of meters or shallower in depth over this region; on the other hand, west of Luzon, SCS can reach more than 5000-m depth. Comprising several archipelago clusters of mostly small islands, SCS has abruptly varying bathymetry even in the deep ocean region. Meanwhile, TC landfall can cause violent vertical mixing in the nearshore shallow water area, making it easy to violate the Courant–Friedrichs–Lewy (CFL) criteria due to dense layering of vertical (sigma) levels in ROMS.

Considering the above, the shallowest depth for ROMS+SWAN D01 is set to be 10 m. Besides, for short timescales, the deep ocean below the thermocline cannot influence the atmosphere or even the upper ocean; the deepest bathymetry was thus lifted to 3000 m. Besides, to ensure numerical stability, the bathymetry was smoothed by applying a linear programming (LP) tool with minimum modification of the actual ocean bottom topography (Sikirić et al. 2009). Figure 3b shows the changed bathymetry using the LP tool in ROMS+SWAN D01. The most significant change occurs within very limited grids close to the shoreline, where the model bottom topography is truncated to smooth the sigma slopes. The number of modified grids is only 5% of the total grids within ROMS+SWAN D01.



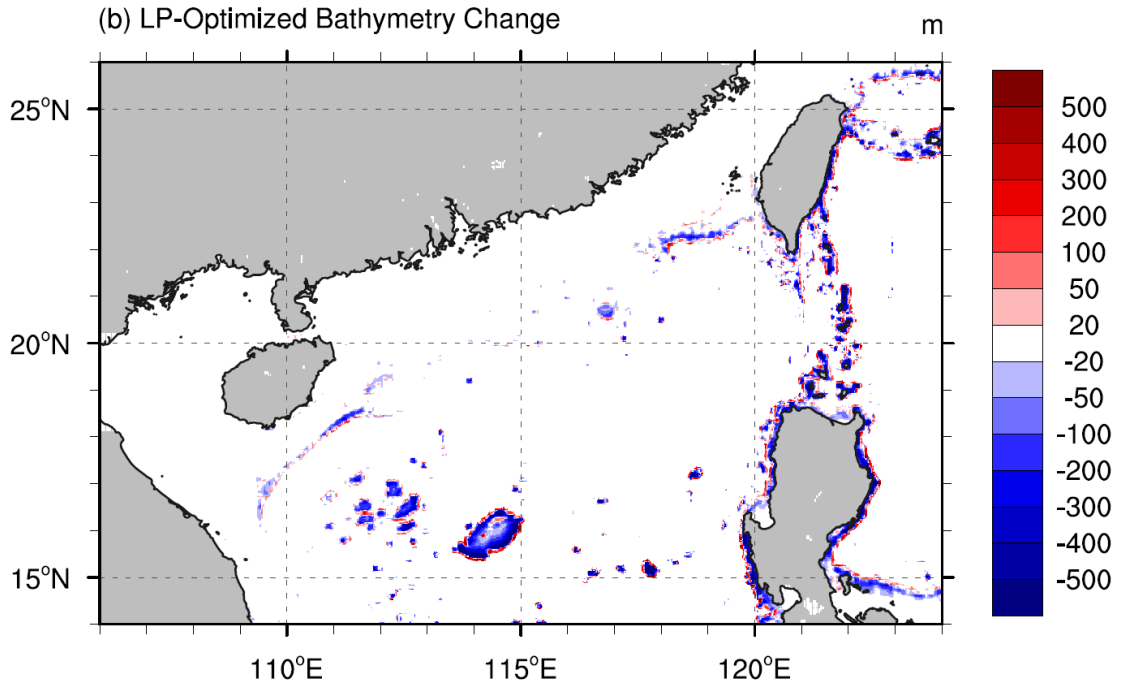


Figure 3 (a) Domain configurations for the ROMS/SWAN. Shading denotes terrain height and bathymetry. The red dashed box illustrates the WRF D02 boundary, and the red dots represent the four observation buoy sites. (b) Difference between the actual and optimized terrain in ROMS/SWAN based on Linear Programming (with positive values for lifted, negative for chopped bathymetry). Bathymetry deeper than 3000 m is lifted to 3000-m depth.

Configurations in each of the three component models are summarized in Table 1. In WRF, the ECMWF L50 standard vertical layers were implemented in the sigma-p hybrid coordinates (<http://www.ecmwf.int/en/forecasts/documentation-and-support/50-model-levels>). ECMWF Reanalysis data version 5 (ERA-5) at $0.25^\circ \times 0.25^\circ$ were used to provide initial and lateral boundary conditions (Hersbach et al. 2020; <https://www.ecmwf.int/en/forecasts/datasets/reanalysis-datasets/era5>). WRF has been spun-up for 24 hours from 12 UTC September 13, 2018, with an intensified initial vortex suitable for the super typhoon being inserted (extracted based on the National Centers for Environmental Prediction final operational (FNL) global 0.25° analysis data). To ensure the large-scale steering flow in the model environment was the same as the observed, hourly spectral nudging, configured in 900-km wavelength and restricted in 400-hPa or higher levels, was turned on in WRF D01 during model integration (see Chen et al. 2020). For the planetary boundary layer physics, the Mellor-Yamada-Janjic Turbulence Kinetic Energy (MYJ TKE) scheme was used (Janjić 1994), which is the default scheme with Air-Wave coupling effect parameterized in

COAWST. The initial and boundary conditions for ROMS were obtained from 1/12° HYbrid Coordinate Ocean Model (HYCOM) reanalysis data (Cummings and Smedstad 2013; <https://www.hycom.org/data/glbv0pt08/expt-93pt0>). The tidal forcing was turned off for stability consideration. In ROMS, 30 sigma layers were constructed and the top 12 levels residing in the upper 200 m of the ocean to represent fine features in the mixed layer. The Generic Length Scale (GLS) mixing scheme (Warner et al. 2005) is adopted to represent the vertical mixing process in the mixed layer, with eddy viscosity and diffusivity coefficients computed according to stability function by Kantha and Clayson (1994). The SWAN model shares the same domain area and spatial resolution with ROMS. Spectral initial and boundary conditions for the former one was obtained from National Oceanic and Atmospheric Administration (NOAA) WaveWatch III 30 arc-minute hindcast data (ftp://polar.ncep.noaa.gov/pub/history/waves/multi_1/201809/gribs/). At each grid point of SWAN, there are 36 10°-directional bins, and wave periods ranging from 1 s to 25 s, evenly separated by 1 s. Thus, for a single grid at the sea surface, the SWAN kernel calculates 36×24 potential wave components in different directions and frequencies. Wind-induced open sea wave breaking (whitecapping) is parameterized by Komen et al. (1984) depending on the mean spectral steepness. Nearshore depth-induced wave breaking (shoaling) is turned on and parameterized when the bathymetry is shallower than 0.73 times of the wave height. Bottom friction in shallow water locations is parameterized by Madsen et al. (1995).

Finally, for atmosphere-wave coupling pertaining to TC wind conditions, the key process is the surface roughness modulation by sea waves, which in turn determines the surface flux exchange coefficients between the atmosphere and the ocean. TY2001 (Taylor and Yelland 2001) is chosen as the default surface roughness scheme, which is embedded in the MYJ TKE planetary boundary layer and associated surface layer scheme over the coupled region. The original MYJ scheme uses a bottom roughness length scale computed based on the stress:

$$z_0 = c_a u_*^2 / g + 0.11\nu / u_* \quad (3-1)$$

where z_0 is the surface roughness length, c_a is the Charnock coefficient (0.018 in MYJ scheme) which is an empirical coefficient for rapidly rising seas (Moon et al. 2004). u_* is the frictional velocity, g the gravitational acceleration, and ν the molecular diffusivity for momentum. In TY2001, the effect of sea state on wind stress is parameterized by wave steepness using the formula:

$$z_0 = 1200 H_s \left(\frac{H_s}{L_p} \right)^{4.5} + 0.11\nu / u_* \quad (3-2)$$

where H_s is the significant wave height, L_p is the peak wavelength.

Over the extreme typhoon-controlled sea surface, wave breaks, sea sprays, air-flow separation, and other nonlinear processes that control surface friction prevail at the extreme high-wind and young-sea state. Considering such a nonlinear effect, another surface roughness scheme C2008 (Caulliez et al. 2008) based on

wave age parameters has been coded into the coupled system in comparison with the default TY2001, to reflect the high-wind-and-young-sea state caused by TC. The effect of sea state on wind stress is parameterized by wave steepness in the following formula:

$$z_0 = 0.0045 (k_p)^{-1} \exp(-0.23C_p/u_*) \quad (3-3)$$

Where k_p is the peak wavenumbers, and C_p is the peak wave phase speed. Both roughness lengths produced by TY2001 and C2008 schemes are restricted under the ceiling value of 0.00285 m (Davis et al. 2008). Such parameterization of sea waves is admittedly simplistic in its representation of the sea state effect. Under tropical cyclones, wave spectra tend to be multi-peaked, hence the peak wavelength will not be a very stable estimate (Janssen et al. 2004).

To understand various coupling effects, four experiments in hierarchical coupling configurations were designed and performed (see Table 2). TY2001 and C2008 are fully coupled AWO simulations with the two different wave-roughness schemes. WRFROMS represents the Atmosphere–Ocean (AO) coupled run without involving SWAN model, and WRFONLY is the atmosphere standalone simulation by WRF model. To better illustrate the results, TY2001 and C2008 are collectively referred to as AWO runs when compared with WRFROMS, referred to as the AO run.

2.3 Observational datasets

Observational data are used to evaluate the performance of the coupled system. Both HKO (<https://www.hko.gov.hk/en/informtc/mangkhut18/mangkhut.htm>) and China Meteorological Administration (CMA, <http://tcdata.typhoon.org.cn/en/tcsize.html>) best track data for Mangkhut (2018) were analyzed. The two best track data sets both provide 3-hourly (or hourly approaching landfall) TC positions, minimum sea-level pressures (SLP) and maximum surface wind speeds data. CMA estimates maximum sustained wind over a 2-minute period, while HKO estimates that over a 10-minute period. When comparing TC maximum wind from model simulations and observations, the following adjustment has been performed: WRF instantaneous wind speed output can be considered as average, with averaging time equivalent to the advective timescale across a grid box. For the 3-km resolution WRF D02 with typical 40 m s^{-1} TC surface wind speed, $\sim 3000/40 \text{ s} = 75 \text{ s}$, which comparable with 1-min averaged wind speed. According to the guideline from World Meteorological Organization, 1-min averaged wind speed can be multiplied by the conversion factor of 0.93 to obtain the 10-minute averaged wind speed (Harper et al. 2010), in alignment with HKO best track data. In-situ wave buoy observations from South China Sea Branch of State Oceanic Administration (SCSB-SOA), China (<http://g.hyyb.org/systems/HyybData/DataDB/>) were downloaded and used to verify oceanic outputs from the coupled model.

Simulation basics and verification of the coupled modeling system

We first evaluate the performance of various modeling systems in capturing super typhoon Mangkhut's characteristics over SCS. The simulated storm tracks from each of the four experiments, along with the HKO and CMA best track, are compared in Fig. 4. Variations in Mangkhut's track with different coupling configurations are relatively minor, indicating that the TC track mainly depends on large-scale atmospheric steering flow and less likely affected by ocean-atmosphere interaction. The experiment best representing the TC track was the TY2001 experiment with AWO fully coupled configuration. The difference in the track errors among the four experiments is quite small (20~30 km) throughout the simulation period. The above results agree with Zambon et al. (2014a) in studying the Atlantic hurricane Ivan (2004). All experiments simulated the same landfall time, which was one hour later (10 UTC September 16, 2018) than the observed one (09 UTC September 16, 2018).

Observational and Simulated Tracks of Mangkhut (1822)

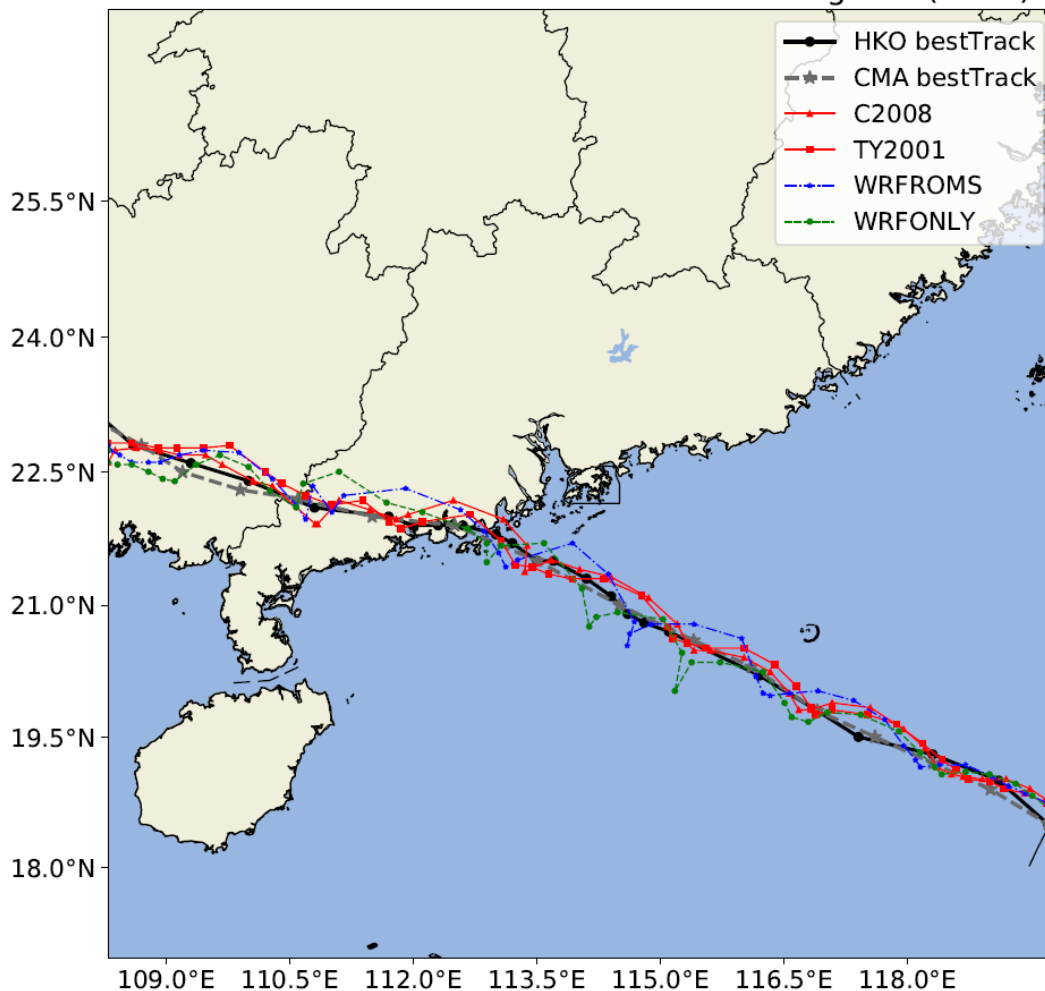
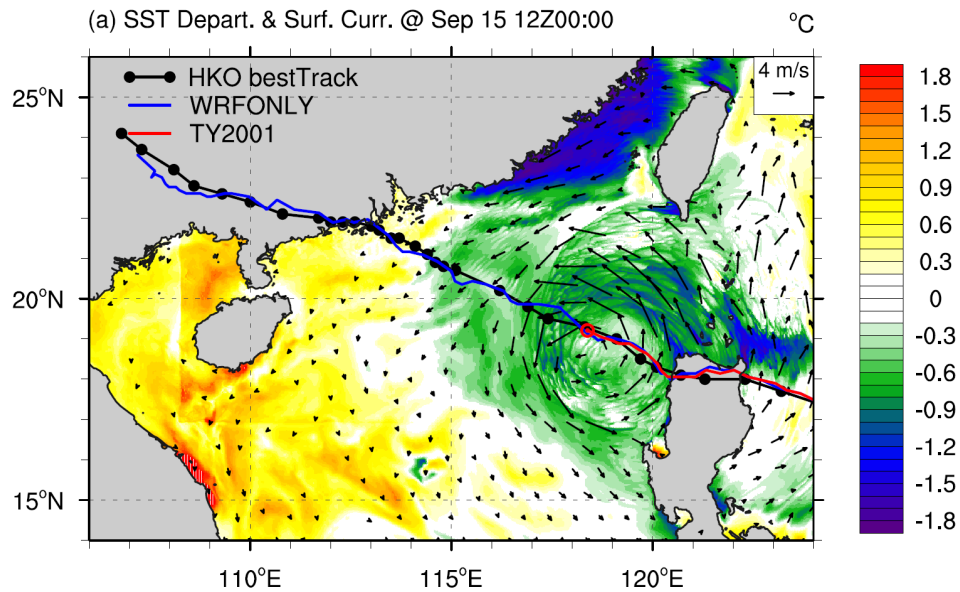


Figure 4 Observational and simulated tracks of Mangkhut (1822) in WRF D02 from Hong Kong Observatory (HKO) best track, China Meteorological Administration (CMA) best track, WRFONLY, WRFROMS, TY2001, and C2008.

Figure 5a shows simulated Sea Surface Temperature (SST) spatial departure from the mean over the whole domain, and ocean surface current at 12 UTC September 15, 2018, from the experiment TY2001. SST cooling (cold wake) can be clearly seen in the vicinity of the TC passage. Remarkable cold anomalies are found to the right (dangerous semicircle) of the moving TC, with maximum signal attaining -1.5 to -2.0 °C. Meanwhile, the swirling surface inflow of the TC drives swirling sea surface currents. Due to the Coriolis effect, the wind-driven rotating water is moving at right angle to the wind direction, outflowing from

the TC center. This divergent Ekman transport induced upwelling and surface heat loss due to turbulent mixing under fierce wind, are responsible for the formation of TC cold wake on the right-hand side of the system. Accordingly, strongest oceanic surface currents exist here. An intriguing feature is that on the leeward of Luzon and other small islands in the Luzon Strait, enhanced SST cooling can be seen in correspondence with offshore currents. This phenomenon implies the excellent performance of the coupled system, as the complicated oceanic dynamics in coastal regions can be resolved: the strong wind-driven offshore current produces coastal upwelling, which is much stronger than that occurs at open-sea due to lateral obstruction of coast. The simulated SST and sea surface current features are in good agreement with previous studies (Moon et al. 2007; Zambon et al. 2014a; Zambon et al. 2014b; Lee and Chen 2014).



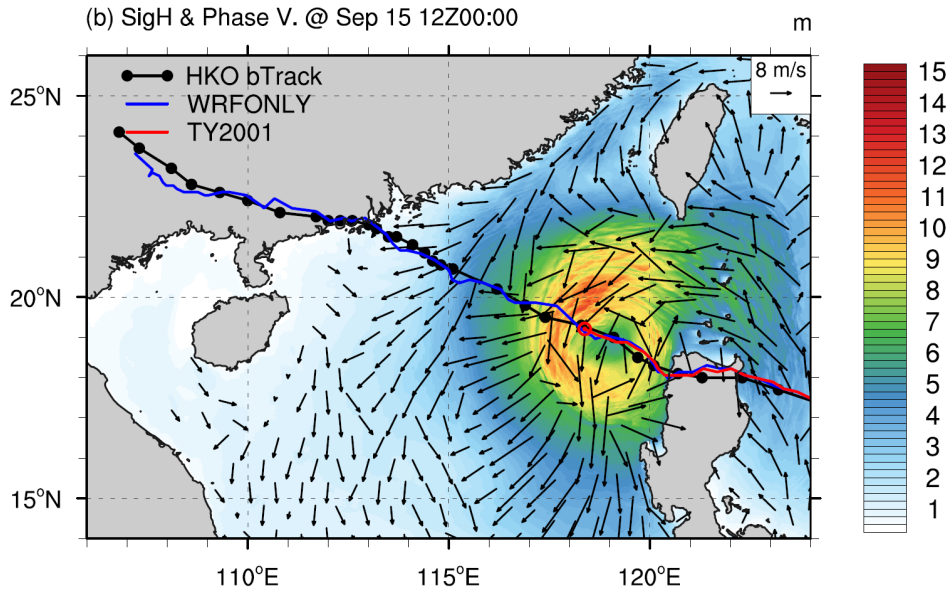


Figure 5 Simulations by ROMS/SWAN at 12Z September 15, 2018 from the experiment TY2001. (a) SST departure ($^{\circ}\text{C}$, shadings) from the mean over the whole domain and ocean surface current (vectors) speed higher than 0.5 m s^{-1} . (b) Same as (a), but for the significant wave height (m, shading), and wind-induced peak wave phase speed (vectors). Tracks of Mangkhut (1822) from HKO best track, WRFONLY, and TY2001 also shown.

Figure 5b gives a comprehensive view of the sea wave field due to strong TC wind. To the right-hand side of the storm, extended fetch length favors the growth of wind waves. Therefore, the highest significant wave height (13-15 m) is observed in the right front quadrant of Mangkhut. High waves also propagate to the left front quadrant of the TC, while the lowest waves are observed in the two rear quadrants, with significant wave height only reaching 7-9 m, about 40% lower than waves in front quadrants. The dominant feature of wind-induced waves in the front half of the TC is wave systems propagating from the right to the left front at the phase speed of about 20 m/s. Young and Burchell (1996) described similar observed wave distribution under a hurricane. To the left-hand side outward from the TC eyewall, TC-generated waves radiate away at the phase speed of 10-20 m/s. These fast-propagating surface gravity waves are seen to cross the SCS basin.

Several ocean and wave related variables are now compared with in-situ wave observations at four buoys (QF303, QF304, QF306, and QF307) located in the continental shelf sea in northern SCS (see Figure 3a), within 100-km distances to the nearest coast, derived from SCSB-SOA, China. Figure 6 shows the comparison of wind speed time series at four buoy locations based on four experiments and observations. All experiments can capture surface wind speed evolution at

four buoy sites. Not only does the atmospheric standalone run (WRFONLY) perform well, the AO coupled or AWO coupled simulations are also in good agreement with the observed wind speed. However, large discrepancies between all simulated results and observations can be found at QF304. As QF304 is adjacent to the domain boundary of WRF D02 (see Figure 3a), such deviations are likely due to boundary nudging in WRF model.

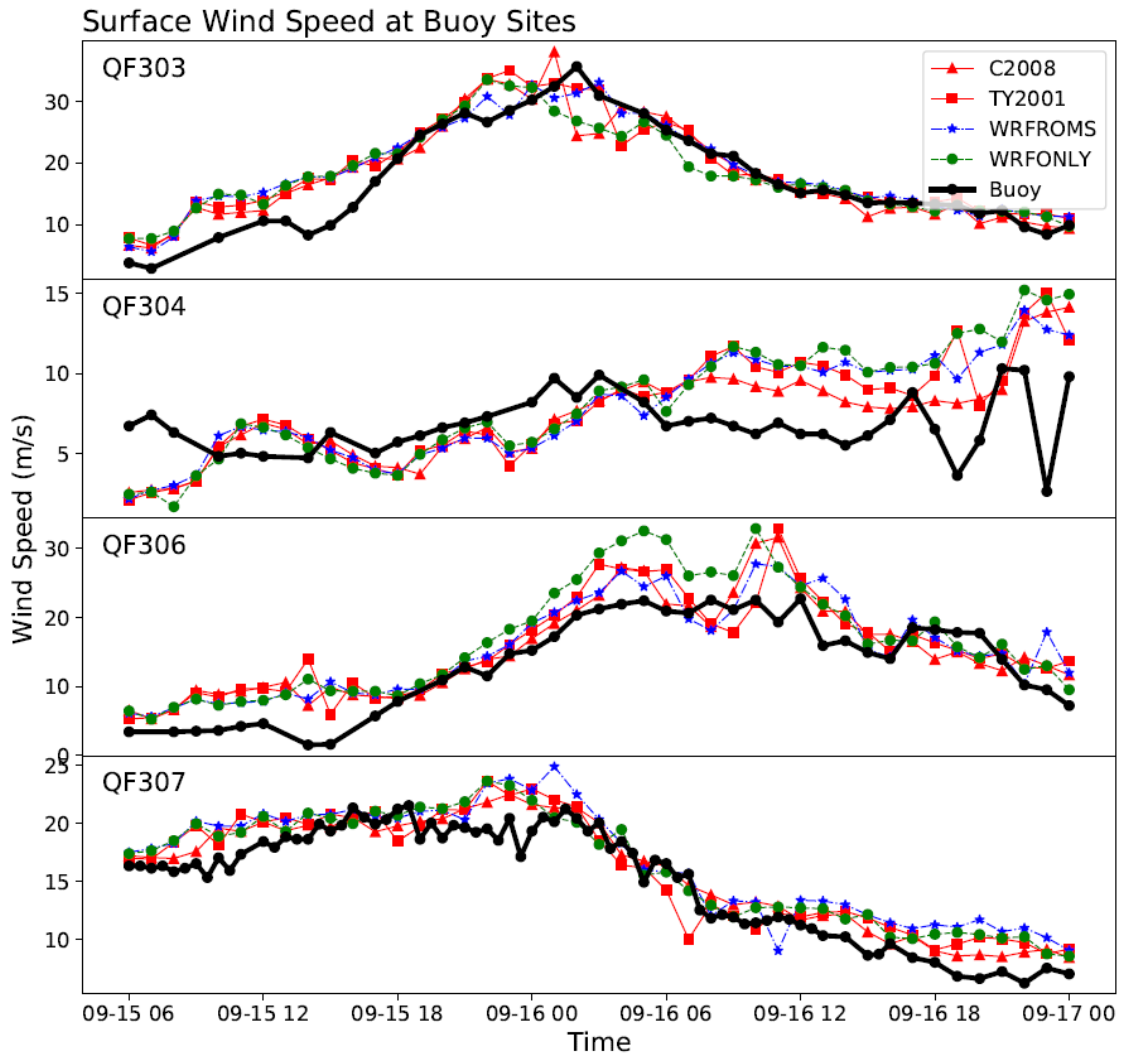


Figure 6 Surface wind speed (m/s) time series from model simulations based on WRFONLY, WRFROMS, C2008, and TY2001 (colored lines) and observations (black line) at buoy site QF303, QF304, QF306 and QF307.

Fig. 7 gives significant wave height time series at four buoy sites in AWO runs. Both TY2001 and C2008 show good performance at QF303, albeit with

its maximum magnitude being underestimated. At QF304, a phase offset is found in the two AWO runs, similar with the situation in wind speed. Model and observed significant wave height are in good agreement at QF306, both in terms of their magnitude and timing. At QF307, although the AWO runs can capture the timing, the simulated wave height is underestimated by 30%. As QF307 is the furthest buoy along the TC's passage, the underestimated magnitude at QF307 may come from the effect of underestimated TC intensity (see Section 4). Overall, both the TY2001 and C2008 AWO coupled simulations can reasonably capture the significant wave height time series.

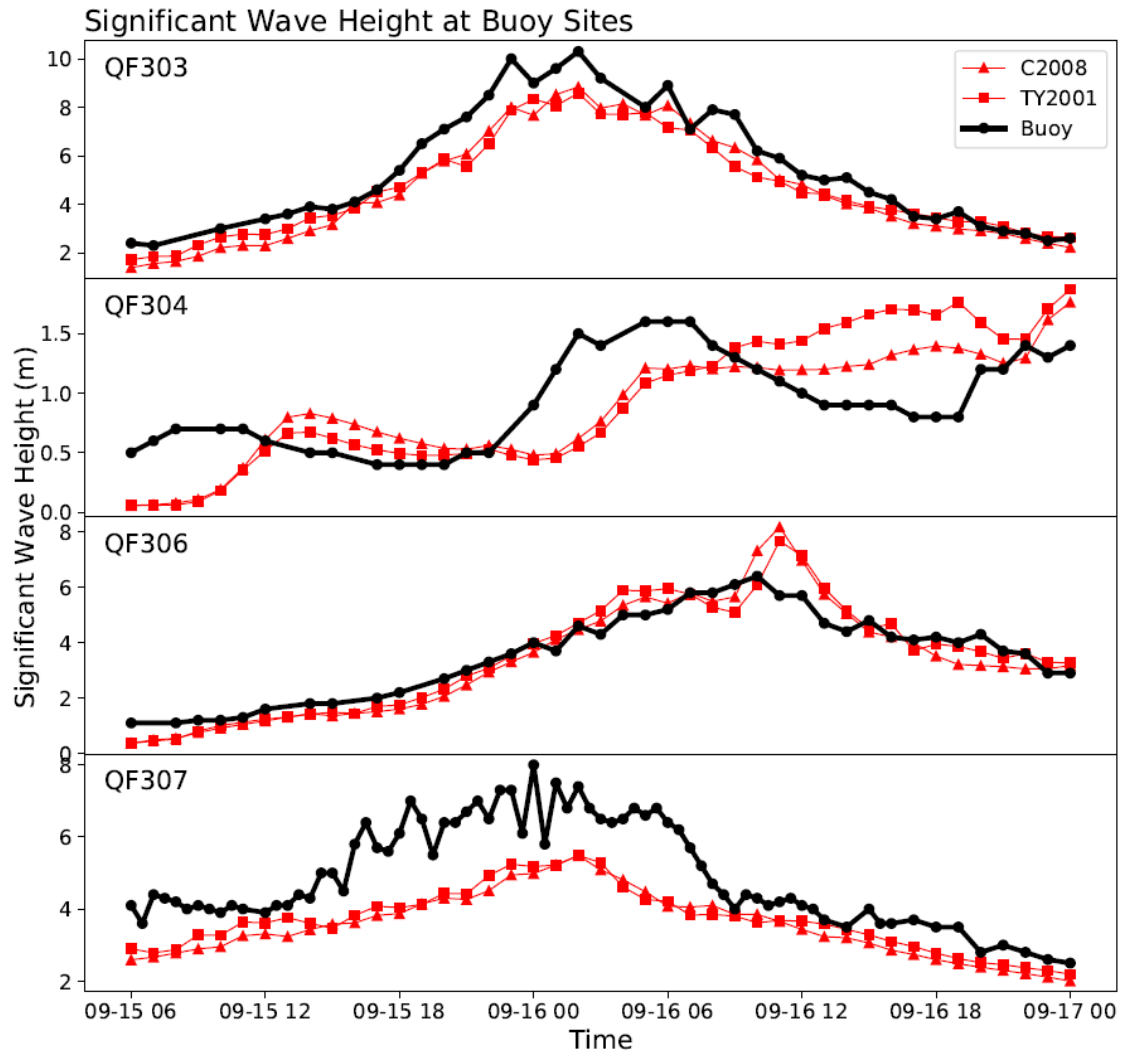


Figure 7 Same as Figure 6 except for significant wave height (m), with simulation based on C2008 and TY2001.

Table 3 summarizes the root-mean-square error (RMSE) for different physical variables at QF303, QF306 and QF307. (Note that QF304 is excluded due to its proximity to the domain lateral boundary.) As seen from the RMSE result, most of selected variables agree well between simulations and observations. For wind speed, AO and AWO runs show reduced RMSE compared with WRFONLY; this is due to the overestimation in WRFONLY (see Fig. 6). For surface pressure, TY2001 provides the best estimation at three buoy sites. AO and AWO runs show similar capabilities in simulating the SST time series, with the RMSE of ~ 1.2 °C. For significant wave height, TY2001 performs slightly better than C2008. The results above demonstrate that the coupled system can reproduce in high fidelity TC characteristics, including strong surface winds, oceanic cold wake, and wind-driven waves.

Compensating TC maximum wind deficit by AWO coupling

The intensity of the simulated TC, determined by either the maximum sustained wind speed (maximum wind) at 10-m height within the cyclone or the minimum surface pressure in the center of the cyclone (central pressure), is the other fundamental quantities in addition to the track. Fig. 8 compares minimum sea level pressure (SLP) and maximum 10-m wind speed from model simulations and HKO best track data. Even initializing the vortex by inserting the intensified TC in FNL data, none of the experiments can reach the pressure drop as deep as the observed SLP. This is believed to be a common bias of current atmospheric models; even in convection-permitting resolution, the grid size still limits the ability to simulate intense cyclones due to the sharp gradient in the core (Prein et al. 2015; Magnusson et al. 2019). Specifically, when the TC was at the open sea (06 UTC September 15–09 UTC September 16), WRFONLY simulates a stable minimum SLP ranging from 955–960 hPa, still 10–15 hPa higher compared with the observed central pressure. Mangkhut in AO and AWO coupled runs exhibits a weakening trend before landfall, in which the SLP increases around 7 hPa. This trend is consistent with the observed TC central pressure evolution, which presents 5 hPa rise before landfall, albeit the mean value is 15 hPa lower. Although WRFONLY simulated TC central pressure is much closer to the observed values, this lack of weakening trend is found before making landfall. As WRFONLY uses the prescribed SST, which can be treated as a fictitious infinite source of heating to the atmosphere, the lack of cold wake effect in the coastal seas off southern China causes the absence of pre-landfall weakening. Magnusson et al. (2019) reported similar phenomena in simulating Atlantic hurricane Irma (2017) using the ECMWF operational coupled model. After making landfall, the TC rapidly weakens in all experiments. Additionally, the TC in AWO coupled runs keep 2–3 hPa deeper compared with AO coupled run. There is no significant difference between simulations using C2008 or TY2001 wave-roughness length schemes. Therefore, despite the underestimated mean value, by introducing an interactive ocean, the coupled runs can more accurately capture the evolutionary trend of TC intensity, especially when Mangkhut experienced weakening as it approaches southern China. A similar effect in AO and AWO coupling has been documented by Zambon et al. (2014a)

in studying the Atlantic hurricane Ivan (2004).

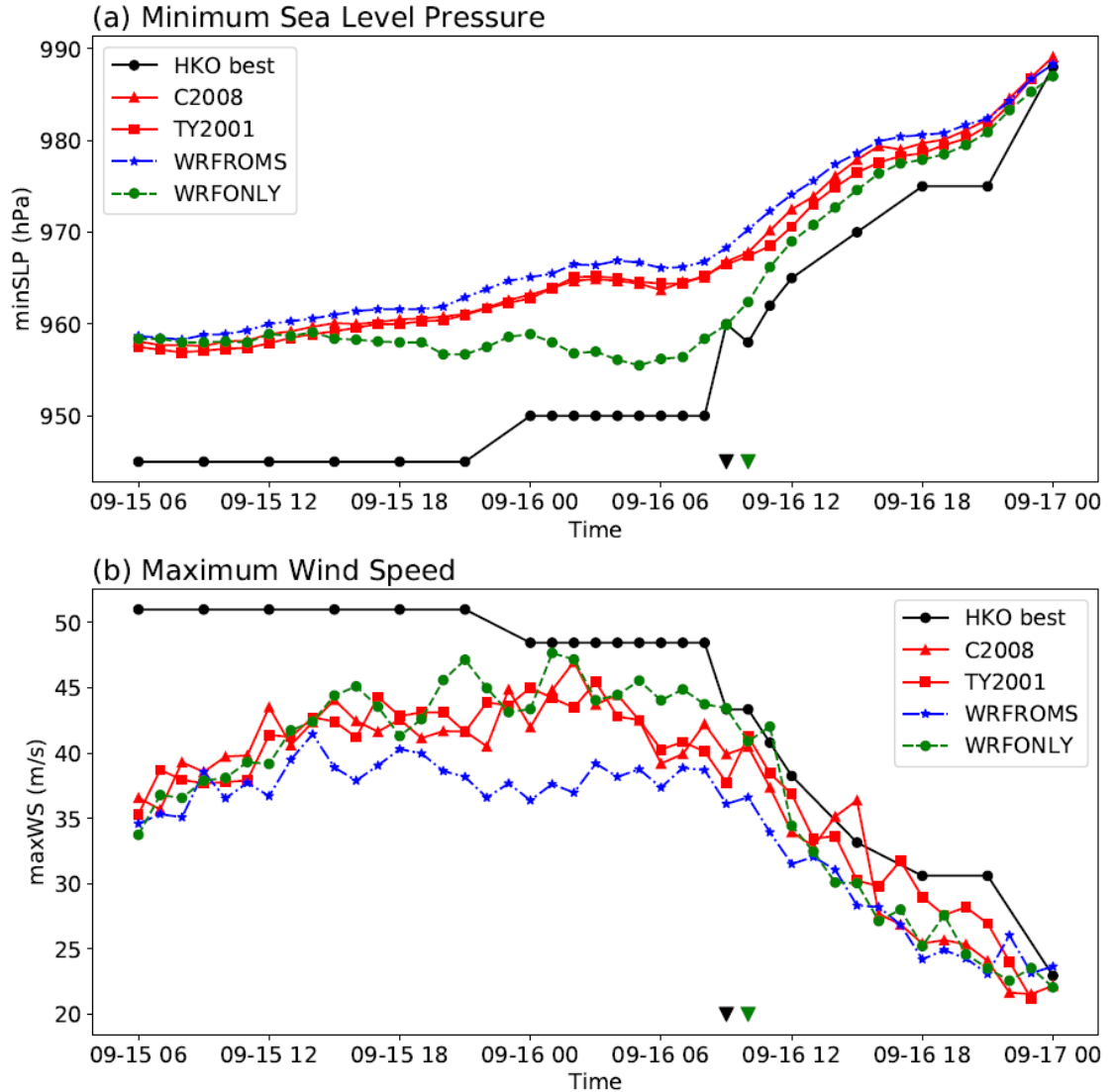


Figure 8 (a) minimum Sea level pressure (hPa) and (b) maximum surface wind speed (m/s) in WRF D02 from model simulations based on WRFONLY, WRFROMS, C2008, and TY2001 (colored lines) and HKO best track data (black line). The black and green upside-down triangle denotes the TC landfall time in HKO best track and simulations, respectively.

Figure 8b shows that, in correspondence with the central pressure, all simulations underestimated the maximum wind before the TC making landfall. Note that the simulated wind speed has been adjusted according to the 10-min aver-

age period based on observation (see Section 2). Besides, discrepancies between simulations and observation during the first several hours resulted from the initial condition and domain lateral boundary effect. The most remarkable feature in Fig. 8b is that, before making landfall, the simulated maximum wind in WRFROMS is around 7 m s^{-1} smaller than WRFONLY. However, note that the “wind speed deficit” is completely compensated in the fully coupled AWO runs, reaching the magnitude close to the atmosphere-only simulations driven by prescribed SST. This feature implies that, the friction at the sea surface is sea-state dependent and tends to decrease to maintain the high surface wind speed. Meanwhile, note that Fig. 8a shows no significant difference in central pressure between the AWO and AO simulations. The results above suggest that, at least in the TC eyewall with extreme high wind speed, introducing coupling of the atmosphere with the wave model tends to decrease the drag coefficient as well as maintaining the heat exchange.

Since TC maximum wind can only reflect limited information about the complicated three-dimensional system, we further investigated the spatial distribution of surface wind speed by conducting TC composite (Figure 9). The composite is based on a 6-hourly average from 18 UTC September 15 to 00 UTC September 16, 2018, during which the WRF D02 could completely contain the TC. Moreover, we confirmed that, during the composite period, the surface is all ocean within 240 km of radius from the TC center. As expected, WRFONLY shows the strongest surface wind due to prescribed SST as the lower boundary condition. The highest wind speed is observed in the right front of the TC eyewall, with wind speed larger than 30 m/s in several patches of area. Due to the cold wake SST feedback (Schade and Emanuel 1999), in WRFROMS, the simulated surface wind speed is much weaker. The wind speed within the eyewall is $5\text{-}7 \text{ m s}^{-1}$ weaker than that in WRFONLY. Interestingly, in TY2001 and C2008, although the distribution is not as compact as in WRFONLY, the simulated wind intensity in the eyewall mimics the magnitude in WRFONLY. This feature confirms that introducing air-wave coupling can compensate the SST feedback that weakens TC wind intensity, especially in the eyewall, where the most intense wind is found.

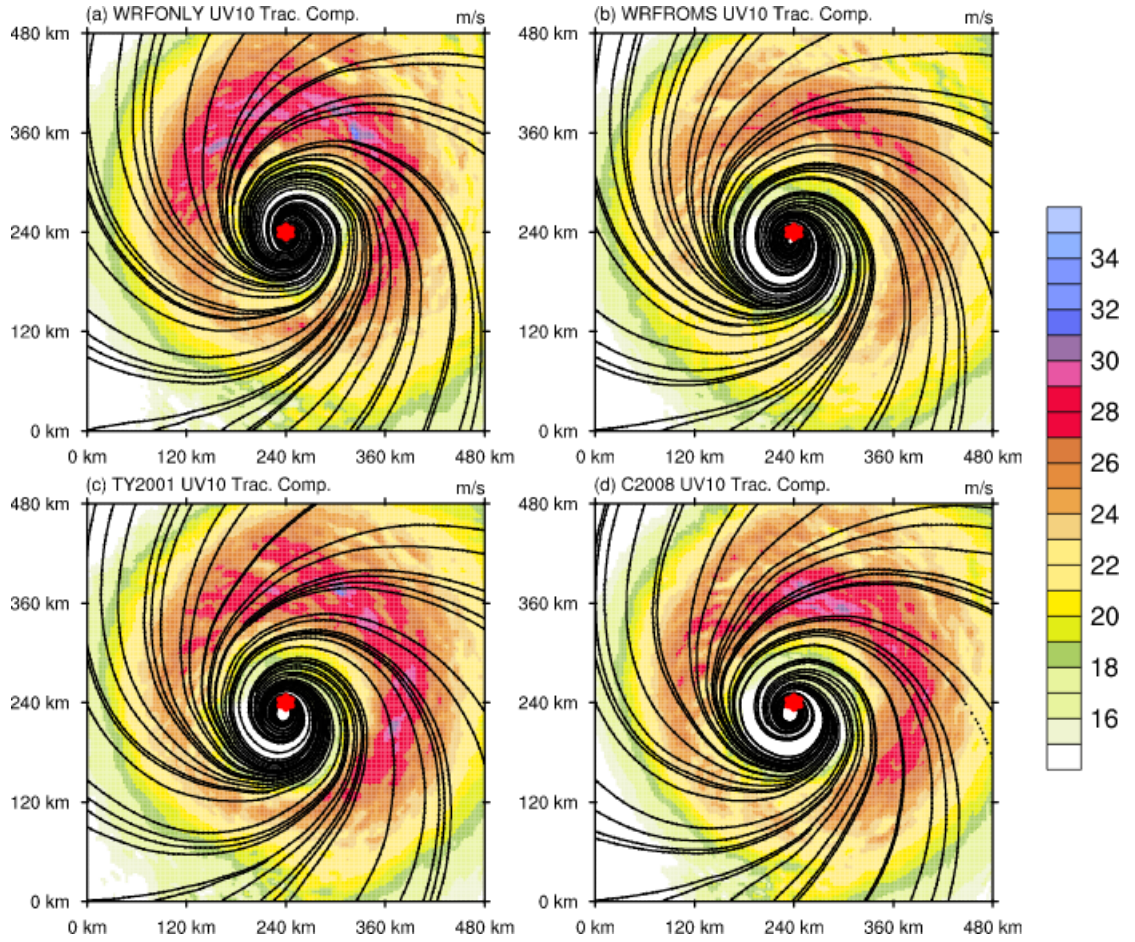


Figure 9 TC composite wind speed (m s^{-1}) and streamlines based on simulation averaged from 18Z September 15 to 00Z September 16, 2018 for (a) WRFONLY experiment. (b) WRFROMS, (c) TY2001, and (d) C2008, respectively.

To further compare the TC wind distribution, Fig. 10 shows the azimuthally averaged wind speed as a function of distance from the TC center, based on TC composites. Stepwise differences among experiments are found in the composites. Within the TC eye (0–40 km from TC center), the averaged wind speed in WRFONLY is around 3 m/s lower than those in AO and AWO coupled run, which is in correspondence with stronger intensity and deeper eye of the simulated TC in WRFONLY. The pattern becomes complicated within the range of 40–120 km from TC center; WRFONLY keeps a nearly constant increase in wind speed as a function of distance with a rate around $0.20 \text{ m s}^{-1} \text{ km}^{-1}$. While for AO and AWO coupled runs, clear stepwise increment in wind intensity is observed: within the range of 40–70 km from TC center, the azimuthally aver-

aged wind speed increases at the rate of $0.13 \text{ m s}^{-1} \text{ km}^{-1}$, which is 35% slower compared with WRFOONLY. Interestingly, within 70 to 120 km from TC center, the wind speed performance in AWO and AO split. For AWO experiments, the wind speed increases from 15 m s^{-1} to 26 m s^{-1} , while for AO is much slower, only up to 22 m s^{-1} at 120 km from TC center. The most intense surface wind distributes at the range of 120–150 km, in which the WRFOONLY and AWO experiments attain the maximum azimuthally averaged wind speed of 26–27 m s^{-1} ; while the AO can only reach 23 m s^{-1} , which is weaker by $\sim 10\%$ or more. For the regions farther than 150 km away from the TC center, surface wind speed in all experiments converges and obtains a similar decline rate with the increment in radius. Azimuthally averaged wind distribution indicates the most notable differences between AO and AWO runs are in the eyewall, which implies the friction in intense wind scenario depends more on the sea state rather than surface wind speed (Powell et al. 2003).

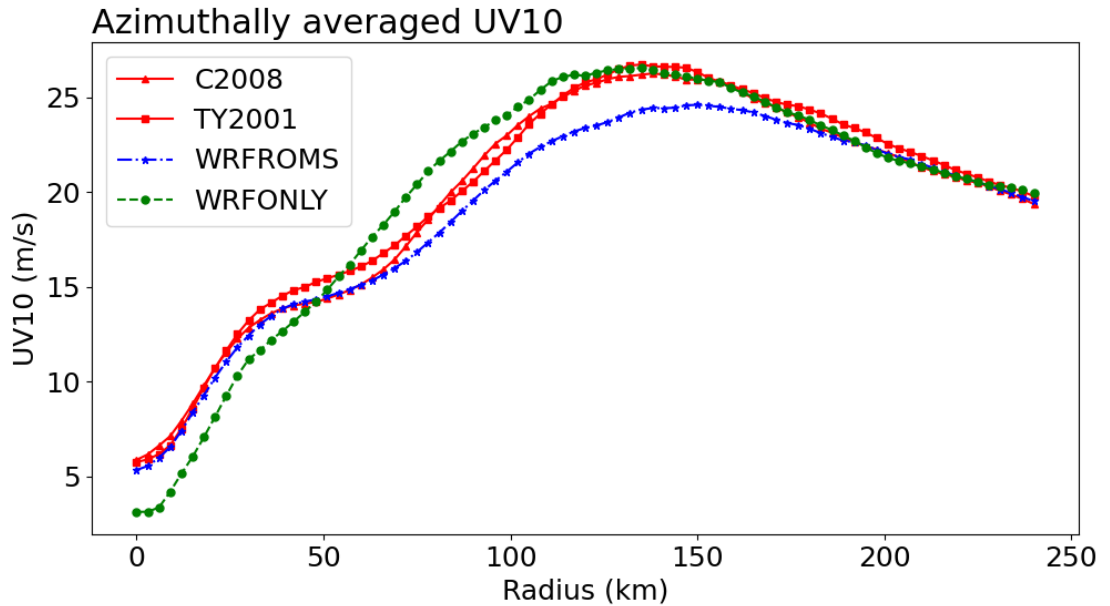


Figure 10 Azimuthally averaged wind speed (m s^{-1}) as a function of distance (km) from the TC center, based on TC composites (see Figure 9) for WRFOONLY, WRFROMS, C2008 and TY2001.

Mechanisms of the compensating effect in AWO coupling

Here we try to address how the “wind speed deficit” within the TC eyewall region, as found in the AO run, can be compensated in the AWO simulations. Fig. 11 shows TC composite difference between AWO and AO runs, regarding surface wind speed and friction velocity. Compared with WRFROMS, both

C2008 (Fig. 11a) and TY2001 (Fig. 11b) show 3-5 m/s stronger surface wind in the TC eyewall. This surface wind intensification in AWO runs does not display obvious discrepancies in the TC's left-hand or right-hand sides. However, the spatial distribution of differences in frictional velocity is quite different. In both C2008 and TY2001, a decoupling feature in frictional velocity and surface wind can be observed. Specifically, on the right-hand side of the TC, stronger surface wind in AWO runs does not necessarily correspond to larger frictional velocity: the frictional velocity in AWO runs reaches an asymptotic level with increasing wind speed, leading to a smaller value compared with the AO run on the right-hand side of the TC where wind speed is large. Meanwhile, this surface wind – frictional velocity decoupling feature is not obvious on the left-hand side of the TC. Therefore, the sea state makes a larger contribution in determining the frictional velocity in very high wind speed.

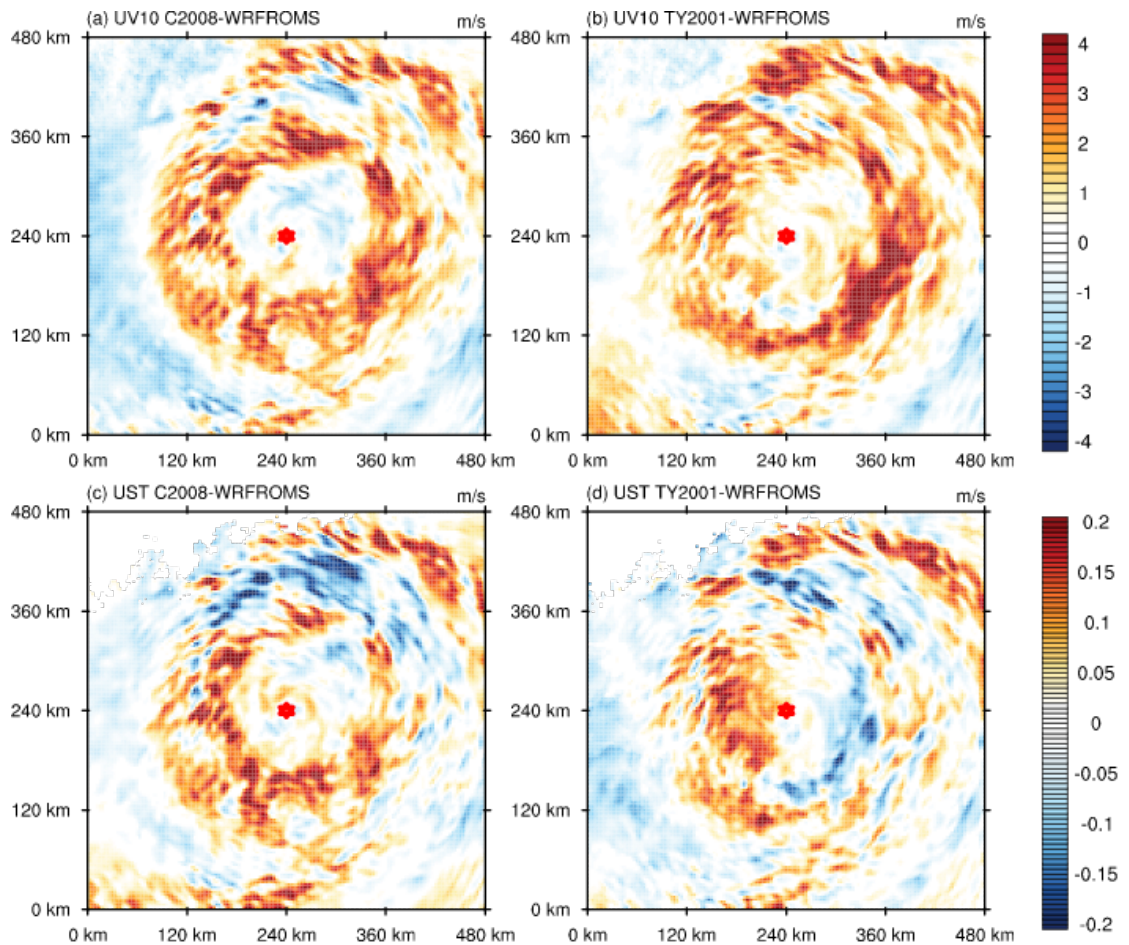
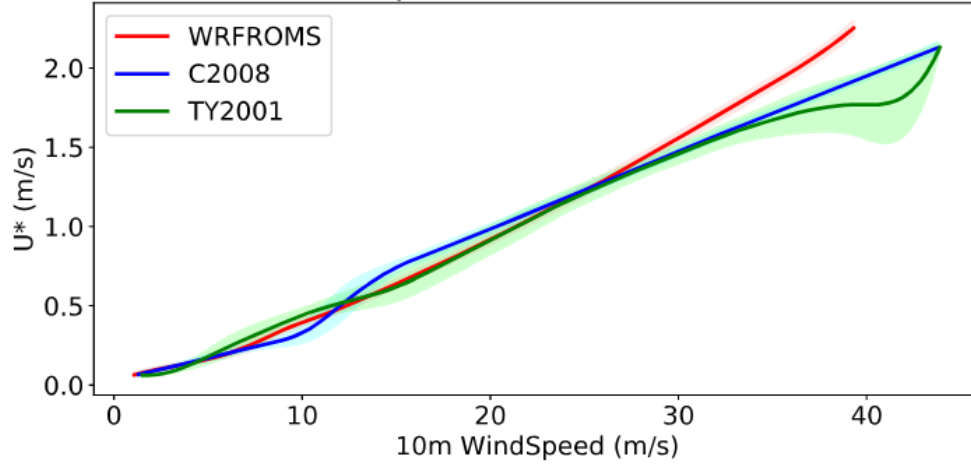


Figure 11 Difference between (a,c) C2008 and WRFROMS, and (b,d) TY2001 and WRFROMS. TC composite results for (a,b) surface wind speed and (c,d)

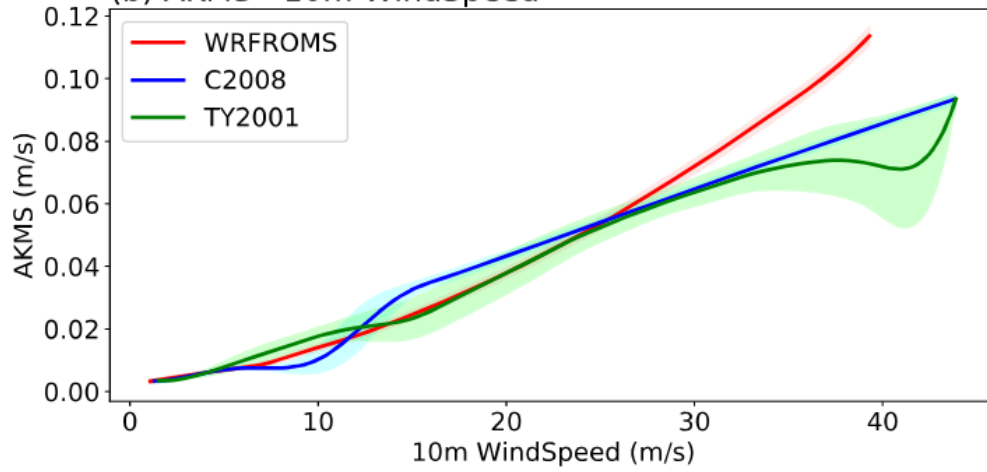
friction velocity. TC composites are computed based on simulations averaged from 18Z September 15 to 00Z September 16, 2018.

We then tested the above hypothesis using binning analysis. Fig. 12 shows frictional velocity, surface exchange coefficients for momentum (AKMS) and heat (AKHS) in MYJ scheme based on TC composites for AO and AWO runs. The growth of frictional velocity as a function of wind speed shows a similar linear relationship, albeit a more complicated pattern in C2008. Remarkably, the frictional velocity increment slows down in AWO runs when the wind speed grows larger than 28 m s^{-1} . In wind speed ranges from 35 m s^{-1} to 42 m s^{-1} , the increment in frictional velocity nearly stagnate in TY2001, with a large variation in possible values for similar wind speeds (see the green shading in Fig. 12a). In addition, TY2001 merges to C2008 at extremely high wind speed ranging from 42 m s^{-1} to 45 m s^{-1} ; this may be due to the limiting value in roughness length by Davis et al. (2008). The momentum and heat flux exchange coefficients are very sensitive to roughness length schemes. In the areas where surface wind speed is larger than 28 m s^{-1} , the bifurcation between AO and AWO experiments expands. A dip in momentum and heat exchange coefficients can be found in TY2001 when the wind speed approaching $40\text{--}42 \text{ m s}^{-1}$. On average, for wind speed larger than 30 m s^{-1} , surface momentum and heat exchange coefficients are reduced by 10–40% in AWO runs than those in AO run.

(a) U^* - 10m WindSpeed



(b) AKMS - 10m WindSpeed



(c) AKHS - 10m WindSpeed

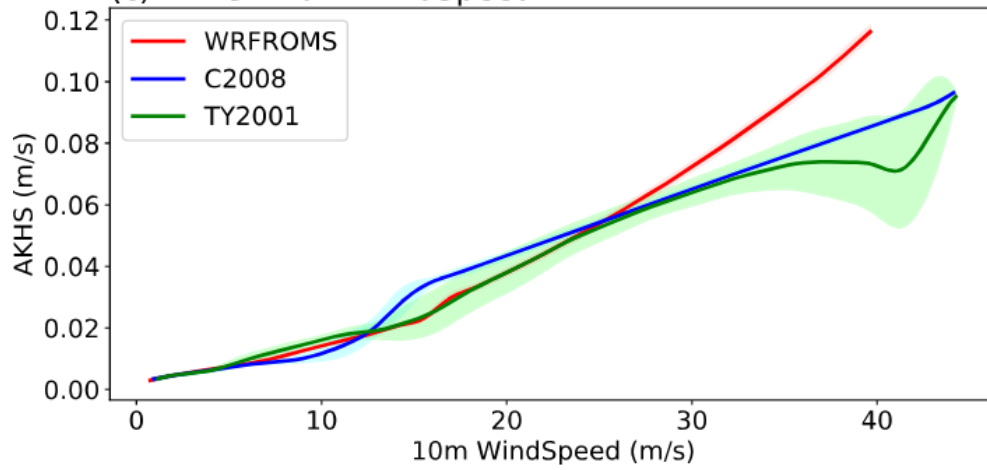


Figure 12 (a) Frictional velocity (m s^{-1}), (b) surface exchange coefficient for momentum (AKMS) and (c) heat (AKHS) in MYJ scheme based on TC composites for WRFROMS, C2008 and TY2001. Shading denotes ± 1 standard deviation ranges. TC composites are computed based on simulations averaged from 18Z September 15 to 00Z September 16, 2018.

The above analysis demonstrates that the sea state determined surface friction can modulate the momentum and heat exchange in high wind speed scenario. The lower momentum exchange coefficient implies the surface wind experiences less drag from the bottom, favoring the flow to maintain its extreme velocity in the TC eyewall. Magnusson et al. (2019) documented similar phenomenon in the ECMWF operational system, in which it is claimed that when the rapidly rotating wind field moves over new patches of the ocean, a perpetual state of young waves can be maintained, thus keeping the cluster of relatively low values of the exchange coefficient for momentum (Magnusson et al. 2019). In our AWO coupled runs, TY2001 and C2008 also capture the above mechanism from both wave steepness and wave age perspectives, respectively. However, as the heat exchange coefficient also decreases as significantly as that observed in the momentum exchange coefficient in high wind speed, one might wonder why the declined heat exchange coefficient at a similar magnitude does not weaken the TC intensity commensurately.

To answer this question, Fig. 13a provides the histograms of surface wind speed in the TC composite box, regarding the AO and AWO runs. A wider distribution function of surface wind speed is seen in AWO runs. In other words, the TC wind in AO run is more concentrated to the area mean wind speed than that of AWO runs. We then separate the wind speed spectrum into three bands according to the intersection points of the three histograms: low wind scenario (wind speed $< 22 \text{ m s}^{-1}$), medium wind scenario ($22 \text{ m s}^{-1} < \text{wind speed} < 28 \text{ m s}^{-1}$), and high wind scenario (wind speed $> 28 \text{ m s}^{-1}$). Compared with AO run, C2008 and TY2001 possess 9% and 5% larger area (grid numbers) in the lower wind scenario, respectively. In the medium wind scenario, AO gains 13% and 11% larger area than C2008 and TY2001. While in the high wind scenario, C2008 and TY2001 obtain 18% and 16% larger area than AO run.

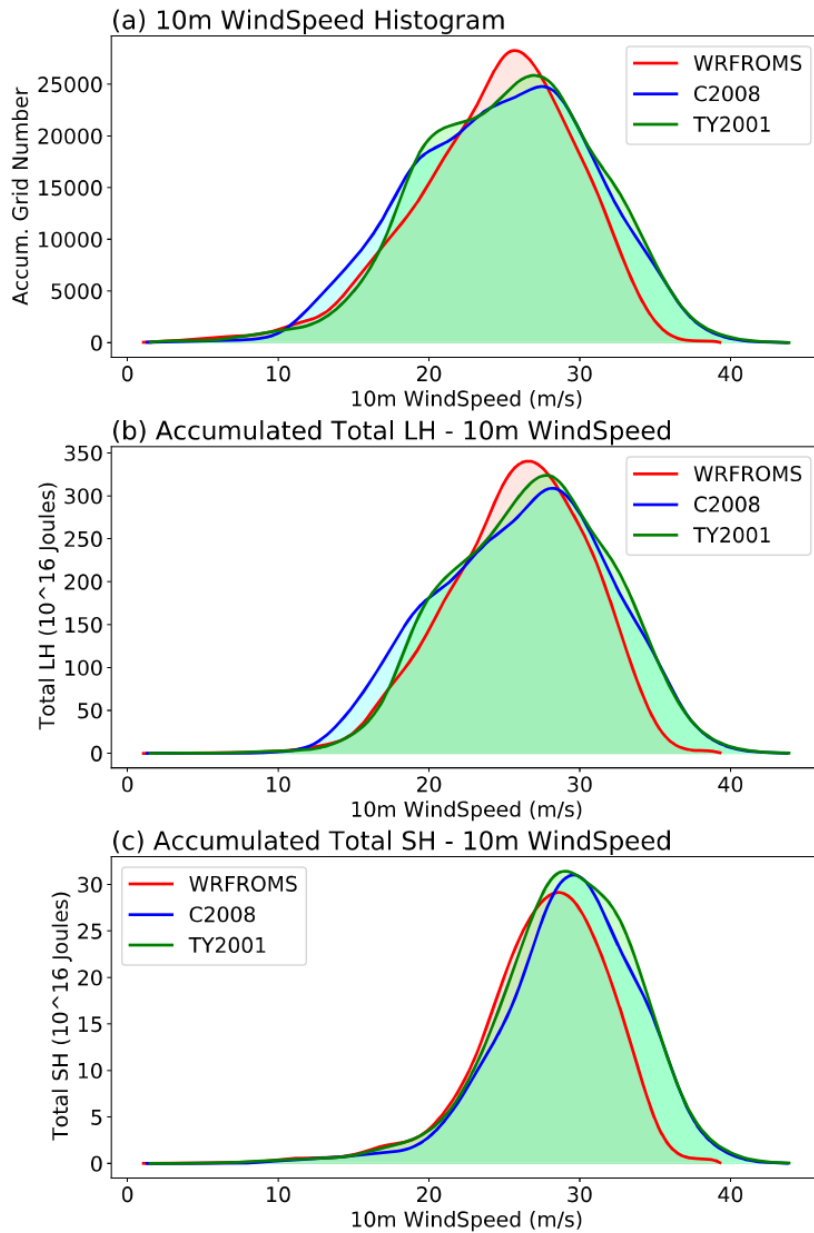


Figure 13 Histogram of (a) surface wind speed (m s^{-1}), (b) accumulated latent heat exchange (10^{16} J) by integrating the latent heat flux over time and area, and (c) accumulated sensible heat exchange (10^{16} J) by integrating the latent heat flux over time and area for WRFROMS, C2008 and TY2001. Original data are binned into 30 equal interval buckets. TC composites are computed based on simulations averaged from 18Z September 15 to 00Z September 16, 2018.

The structural difference of surface wind distribution in AO and AWO runs, especially in the high wind scenario, is expected to modulate the actual absorbed heat from sea surface by the TC. Figs. 13b-c display the histograms of total latent heat (LH) and sensible heat (SH) accumulated by the TC from sea surface, which is calculated by integrating the LH and SH flux weighted by time and area during the TC composite period (unit in 10^{16} Joules). Remarkably, the total LH accumulated by the TC is dominated by the wind speed distribution function, by which the larger area in the high wind scenario completely offsets the reduced heat exchange coefficient in AWO runs. In other words, in AWO runs, the TC receives more LH energy in total due to the larger high wind speed area than that in the AO run. Similarly, AWO runs obtain more LH due to the larger area effect in low wind scenarios. Although AO run obtains more LH in the medium wind scenario, the surplus cannot offset larger deficits in low and high wind scenarios. Overall, AWO runs extracted 7% more LH from the sea surface compared with the AO run. The total SH, which is more sensitive to the wind speed, has no significant difference in the low and medium wind speed scenarios between AO and AWO experiments. In the high wind scenario, both larger area and sensitivity boost much more total SH accumulated by the TC in AWO runs. To be specific, in high wind scenario, the TC absorbs more SH by 24% and 21% in TY2001 and C2008 than that in WRFROMS, respectively. To add up, AWO runs accumulated around 16% more SH from the sea surface than the AO run. Note that SH is nearly one order of magnitude smaller than LH. In any case, the larger area of high wind speed in AWO runs dominates the total LH and SH that the TC obtained from the sea surface, compensating the smaller heat exchange coefficient effect. In total, the AWO runs gain 8-9% more total heat from the sea surface than AO run during the TC composite period. This additional heating, to some extent, compensates the declined intensity that the AO coupling (SST feedback) takes away. In fact, from recent field campaigns (Brut et al. 2005, Cook and Renfrew 2015), the exchange coefficients for heat and moisture may keep growing in high wind scenario than currently simulated ones. Therefore, the reduced momentum exchange coefficients in combination with increased heat and moisture exchange coefficient, is expected to prompt the strong TC to leech much more energy from the ocean, which may work as nonlinear positive feedback to support TC's rapid intensification (Magnusson et al. 2019).

Summary and discussion

TCs are some of the most deadly natural disasters, accurately forecasting TC impacts therefore is crucial for coastal risk assessment and management. The skill of tropical cyclone forecasting has continuously improved over the past few decades; however, capturing the TC intensity still challenges most state-of-the-art operational forecasting systems. By performing a series of numerical simulations based on hierarchical coupling configurations in a coupled Atmosphere–Wave–Ocean (AWO) modeling system, we showed that TC intensity can be sensitive to lower boundary conditions provided by interactive ocean and sea wave models.

We first used in-situ buoy data to verify that the coupled system can reproduce high-fidelity TC-related physical status in each of the three components, including the fierce winds, oceanic cold wake, and wind waves. Further analysis reveals that, although involving the ocean coupling reproduces a realistic TC cold wake, the simulated maximum surface wind speed drops around 7 m/s. While in the fully coupled AWO runs, the wind speed deficit can be completely compensated by the wave-air coupling effect, reaching the magnitude close to the atmospheric standalone simulation driven by fixed SST. For the central pressure, only coupled runs can capture the weakening trend consistent with observation before landfall, albeit 10-15 hPa underestimation. In the AWO runs, benefiting from the better structural representation of surface roughness, two mechanisms contribute to the improvement of TC intensity: 1) Surface drag coefficient reaches an asymptotic level in the high wind scenario ($>28\text{m s}^{-1}$), assisting the TC to maintain extreme wind speed within the eyewall. 2) Wider stretch of wind speed distribution offsets the negative effect due to stagnant increment in heat exchange coefficient, by which the TC extracted 8-9% more total heat from the ocean to maintain its strength. Fully resolved evolution in the ocean and sea state, especially their complicated, nonlinear, and sensitive interactions with the lower atmosphere, is important for the prediction of intense weather systems (e.g., TC). AWO interaction is especially complicated and important within the extremely high winds and strong gradient zones of pressure located in the inner core (eye and eyewall) of a tropical cyclone. The momentum and heat exchange coefficients under the extreme high-wind conditions are very difficult to determine precisely in the regions where they are most important (Chen et al. 2007). It is quite difficult to isolate pure "sea-state dependent" effects from these experiments. As a cap on z_0 exists, the two sea-state dependent models can be influenced by this and ultimately produce similar performance. In any case, in our AWO runs, both wave steepness-based and wave age-based schemes can capture the complicated surface roughness changes near the TC eyewall. Besides, a single case experiment is not an effective approach for describing physics effects in such highly interactive coupled systems as TCs. Ensemble runs are needed in the future to quantify the uncertainties in the results and for better inference of the AOW vs AO effects on TC intensity simulations.

Moreover, recent field campaigns (Brut et al. 2005, Cook and Renfrew 2015) indicated the exchange coefficients for heat and moisture may keep growing in high wind scenarios than currently modeled. Noted that the ratio of surface exchange coefficients, calculated by dividing heat and moisture from momentum exchange coefficient (C_k/C_d), is the key parameter to control the TC intensity (Emanuel, 1995; Bister and Emanuel 1998); thus, the reduced momentum exchange coefficient in combination with increased heat and moisture exchange coefficient, is expected to prompt the strong TC to leech much more energy from the ocean, which may work as nonlinear positive feedback to support TC's rapid intensification (Magnusson et al. 2019). Bell et al. (2012) have confirmed that the ratio of surface exchange coefficients (C_k/C_d) have quite a large range of possible values (from 0.1 to more than 1.0) when the wind speed is larger than

30 m s⁻¹. While for the default MYJ surface layer scheme, the Ck/Cd ratio is determined by a simple empirical relationship with limiting values. Therefore, ongoing work is demanded to quantify the impact of wave-air interaction on the ratio of surface exchange coefficients by simulating several TCs in different regions with various strengths. It is worth emphasizing that such knowledge would not be possible without interactive ocean and sea wave models. As can be seen in the ECMWF operational model, coupling the atmosphere, land surface, sea wave, and 3-D ocean not only provides a more realistic representation of physical mechanisms, but also benefits regional storm risk assessment and management. As the coastal residents and environment will be more vulnerable to TC-related disasters under a warning climate, their impacts can be minimized using a range of management approaches, e.g., response, recovery, prevention/reduction, and preparedness (Lin Moe and Pathranarakul 2006; Hoque et al. 2017), in combination with more skillful TC forecasts by regional or global climate models.

Acknowledgements. Y. Li was supported by the National Key Projects of Ministry of Science and Technology of China (2018YFC1506405) and the National Natural Science Foundation of China (Grants 42075072). The Vice-Chancellor’s Discretionary Fund of The Chinese University of Hong Kong (CUHK, Project Number: 4930744, 4930777) also supported this project. C.-Y. Tam is supported by the CUHK Direct Grant (Project Number: 4053427). The appointment of N.-C. Lau at the CUHK is partially supported by the AXA Research Fund. Computing resource was provided by the CUHK Central Cluster. We also appreciate Dr. Mathieu Dutour Sikirić from Ruđer Bošković Institute providing the linear programming tool to modify the ocean bottom topography.

Data Availability Statement All data used during this study are openly available with URL or doi links cited.

Open Research

ECMWF Reanalysis data version 5 (ERA-5) at 0.25°×0.25° in this study is available at <https://www.ecmwf.int/en/forecasts/datasets/reanalysis-datasets/era5> (Hersbach et al. 2020).

1/12° HYbrid Coordinate Ocean Model (HYCOM) reanalysis data is available via <https://www.hycom.org/data/g1bv0pt08/expt-93pt0> (Cummins and Smedstad 2013).

National Oceanic and Atmospheric Administration (NOAA) WaveWatch III 30 arc-minute hindcast data is available via ftp://polar.ncep.noaa.gov/pub/history/waves/multi_1/201809/gribs/.

HKO and CMA best track data are available via <https://www.hko.gov.hk/en/informtc/mangkhut18/mangkhut.htm> and <http://tcdata.typhoon.org.cn/en/tcsize.html>, respectively.

In-situ wave buoy observations from South China Sea Branch of State Oceanic Administration (SCSB-SOA), China is available via <http://g.hyyb.org/systems/HyybData/DataDB/>.

Version 3.6 of the COAWST system used in the study is available via svn repository: <https://coawstmodel.sourcerepo.com/coawstmodel/COAWST>. Username and password will be provided by the developer Dr. John Warner (jcwarner@usgs.gov) upon request.

References

- Bell, M.M., Montgomery, M.T. and Emanuel, K.A., 2012. Air–sea enthalpy and momentum exchange at major hurricane wind speeds observed during CBLAST. *Journal of the Atmospheric Sciences*, 69(11), pp.3197-3222.
- Bender, M.A., Ginis, I., Tuleya, R., Thomas, B. and Marchok, T., 2007. The operational GFDL coupled hurricane–ocean prediction system and a summary of its performance. *Monthly Weather Review*, 135(12), pp.3965-3989.
- Bhatia, K.T., Vecchi, G.A., Knutson, T.R., Murakami, H., Kossin, J., Dixon, K.W. and Whitlock, C.E., 2019. Recent increases in tropical cyclone intensification rates. *Nature communications*, 10(1), pp.1-9.
- Bister, M. and Emanuel, K.A., 1998. Dissipative heating and hurricane intensity. *Meteorology and Atmospheric Physics*, 65(3), pp.233-240.
- Bruneau, N., Toumi, R. and Wang, S., 2018. Impact of wave whitecapping on land falling tropical cyclones. *Scientific reports*, 8(1), pp.1-11.
- Brut, A., Butet, A., Durand, P., Caniaux, G. and Planton, S., 2005. Air–sea exchanges in the equatorial area from the EQUALANT99 dataset: Bulk parametrizations of turbulent fluxes corrected for airflow distortion. *Quarterly Journal of the Royal Meteorological Society: A journal of the atmospheric sciences, applied meteorology and physical oceanography*, 131(610), pp.2497-2538.
- Caulliez, G., Makin, V. and Kudryavtsev, V., 2008. Drag of the water surface at very short fetches: Observations and modeling. *Journal of physical oceanography*, 38(9), pp.2038-2055.
- Chen, J., Wang, Z., Tam, C.Y., Lau, N.C., Lau, D.S.D. and Mok, H.Y., 2020. Impacts of climate change on tropical cyclones and induced storm surges in the Pearl River Delta region using pseudo-global-warming method. *Scientific reports*, 10(1), pp.1-10.
- Chen, S.S., Price, J.F., Zhao, W., Donelan, M.A. and Walsh, E.J., 2007. The CBLAST-Hurricane program and the next-generation fully coupled atmosphere–wave–ocean models for hurricane research and prediction. *Bulletin of the American Meteorological Society*, 88(3), pp.311-318.
- Chen, S.S., Zhao, W., Donelan, M.A. and Tolman, H.L., 2013. Directional wind–wave coupling in fully coupled atmosphere–wave–ocean models: Results from CBLAST-Hurricane. *Journal of the Atmospheric Sciences*, 70(10), pp.3198-3215.
- Cook, P.A. and Renfrew, I.A., 2015. Aircraft-based observations of air–sea

- turbulent fluxes around the British Isles. *Quarterly Journal of the Royal Meteorological Society*, 141(686), pp.139-152.
- Cummings, J.A. and Smedstad, O.M., 2013. Variational data assimilation for the global ocean. In *Data Assimilation for Atmospheric, Oceanic and Hydrologic Applications (Vol. II)* (pp. 303-343). Springer, Berlin, Heidelberg.
- Davis, C., Wang, W., Chen, S.S., Chen, Y., Corbosiero, K., DeMaria, M., Duhia, J., Holland, G., Klemp, J., Michalakes, J. and Reeves, H., 2008. Prediction of landfalling hurricanes with the advanced hurricane WRF model. *Monthly weather review*, 136(6), pp.1990-2005.
- Emanuel, K. A., 1995: Sensitivity of tropical cyclones to surface exchange coefficients and a revised steady-state model incorporating eye dynamics. *J. Atmos. Sci.*, 52, 3969–3976.
- Emanuel, K. and Zhang, F., 2016. On the predictability and error sources of tropical cyclone intensity forecasts. *Journal of the Atmospheric Sciences*, 73(9), pp.3739-3747.
- Emanuel, K., 2003. A similarity hypothesis for air–sea exchange at extreme wind speeds. *Journal of the atmospheric sciences*, 60(11), pp.1420-1428.
- Emanuel, K., 2005. Increasing destructiveness of tropical cyclones over the past 30 years. *Nature*, 436(7051), pp.686-688.
- Harper, B.A., Kepert, J.D. and Ginger, J.D. (2010) Guidelines for converting between various wind averaging periods in tropical cyclone conditions. WMO/TD-1555, pp. 4.
- Hersbach, H., Bell, B., Berrisford, P., Hirahara, S., Horányi, A., Muñoz-Sabater, J., Nicolas, J., Peubey, C., Radu, R., Schepers, D. and Simmons, A., 2020. The ERA5 global reanalysis. *Quarterly Journal of the Royal Meteorological Society*, 146(730), pp.1999-2049.
- Hoque, M. A. A., Phinn, S., Roelfsema, C. and Childs, I., 2016. Assessing tropical cyclone impacts using object-based moderate spatial resolution image analysis: a case study in Bangladesh. *International Journal of Remote Sensing*, 37(22), pp. 5320-5343.
- Hoque, M. A. A., Phinn, S., Roelfsema, C. and Childs, I. 2017. Tropical cyclone disaster management using remote sensing and spatial analysis: A review. *International journal of disaster risk reduction*, 22, pp. 345-354.
- Ito, K., Kuroda, T., Saito, K. and Wada, A., 2015. Forecasting a large number of tropical cyclone intensities around Japan using a high-resolution atmosphere–ocean coupled model. *Weather and Forecasting*, 30(3), pp.793-808.
- Janjić, Z.I., 1994. The step-mountain eta coordinate model: Further developments of the convection, viscous sublayer, and turbulence closure schemes. *Monthly weather review*, 122(5), pp.927-945.

- Janssen, P. and Janssen, P.A., 2004. The interaction of ocean waves and wind. Cambridge University Press.
- Judt, F., Chen, S.S. and Berner, J., 2016. Predictability of tropical cyclone intensity: Scale-dependent forecast error growth in high-resolution stochastic kinetic-energy backscatter ensembles. *Quarterly Journal of the Royal Meteorological Society*, 142(694), pp.43-57.
- Kantha, L.H. and Clayson, C.A., 1994. An improved mixed layer model for geophysical applications. *Journal of Geophysical Research: Oceans*, 99(C12), pp.25235-25266.
- Klotzbach, P.J., 2006. Trends in global tropical cyclone activity over the past twenty years (1986–2005). *Geophysical Research Letters*, 33(10).
- Komen, G.J., Hasselmann, S. and Hasselmann, K., 1984. On the existence of a fully developed wind-sea spectrum. *Journal of physical oceanography*, 14(8), pp.1271-1285.
- Lee, C.Y. and Chen, S.S., 2014. Stable boundary layer and its impact on tropical cyclone structure in a coupled atmosphere–ocean model. *Monthly Weather Review*, 142(5), pp.1927-1944.
- Li D., Staneva J., Bidlot J.-R., Grayek S., Zhu Y. and Yin B., 2021. Improving Regional Model Skills During Typhoon Events: A Case Study for Super Typhoon Lingling Over the Northwest Pacific Ocean. *Front. Mar. Sci.* 8:613913. doi:10.3389/fmars.2021.613913
- Lin Moe, T. and Pathranarakul, P. 2006. An integrated approach to natural disaster management: Public project management and its critical success factors. *Disaster Prevention and Management*, 15(3), pp. 396-413.
- Lloyd, I.D. and Vecchi, G.A., 2011. Observational evidence for oceanic controls on hurricane intensity. *Journal of Climate*, 24(4), pp.1138-1153.
- Madsen, O.S., 1995. Spectral wave-current bottom boundary layer flows. In *Coastal Engineering 1994* (pp. 384-398).
- Magnusson, L., Bidlot, J.R., Bonavita, M., Brown, A.R., Browne, P.A., De Chiara, G., Dahoui, M., Lang, S.T.K., McNally, T., Mogensen, K.S. and Pappenberger, F., 2019. ECMWF activities for improved hurricane forecasts. *Bulletin of the American Meteorological Society*, 100(3), pp.445-458.
- Mogensen, K.S., Magnusson, L. and Bidlot, J.R., 2017. Tropical cyclone sensitivity to ocean coupling in the ECMWF coupled model. *Journal of Geophysical Research: Oceans*, 122(5), pp.4392-4412.
- Moon, I.J., Ginis, I. and Hara, T., 2004. Effect of surface waves on Charnock coefficient under tropical cyclones. *Geophysical research letters*, 31(20).
- Moon, I.J., Ginis, I., Hara, T. and Thomas, B., 2007. A physics-based parameterization of air–sea momentum flux at high wind speeds and its impact on

- hurricane intensity predictions. *Monthly weather review*, 135(8), pp.2869-2878.
- Murakami, H., Vecchi, G.A., Underwood, S., Delworth, T.L., Wittenberg, A.T., Anderson, W.G., Chen, J.H., Gudgel, R.G., Harris, L.M., Lin, S.J. and Zeng, F., 2015. Simulation and prediction of category 4 and 5 hurricanes in the high-resolution GFDL HiFLOR coupled climate model. *Journal of Climate*, 28(23), pp.9058-9079.
- Olabarrieta, M., Warner, J.C., Armstrong, B., Zambon, J.B. and He, R., 2012. Ocean-atmosphere dynamics during Hurricane Ida and Nor'Ida: An application of the coupled ocean-atmosphere-wave-sediment transport (COAWST) modeling system. *Ocean Modelling*, 43, pp.112-137.
- Powell, M.D., Vickery, P.J. and Reinhold, T.A., 2003. Reduced drag coefficient for high wind speeds in tropical cyclones. *Nature*, 422(6929), pp.279-283.
- Prein, A.F., Langhans, W., Fosser, G., Ferrone, A., Ban, N., Goergen, K., Keller, M., Tölle, M., Gutjahr, O., Feser, F. and Brisson, E., 2015. A review on regional convection-permitting climate modeling: Demonstrations, prospects, and challenges. *Reviews of geophysics*, 53(2), pp.323-361.
- Reul, N., Branger, H. and Giovanangeli, J.P., 1999. Air flow separation over unsteady breaking waves. *Physics of Fluids*, 11(7), pp.1959-1961.
- Roy, C. and Kovordányi, R., 2012. Tropical cyclone track forecasting techniques A review. *Atmospheric research*, 104, pp.40-69.
- Schade, L.R. and Emanuel, K.A., 1999. The ocean's effect on the intensity of tropical cyclones: Results from a simple coupled atmosphere-ocean model. *Journal of the Atmospheric Sciences*, 56(4), pp.642-651.
- Schmidt, S., Kemfert, C. and Höpfe, P., 2010. The impact of socio-economics and climate change on tropical cyclone losses in the USA. *Regional Environmental Change*, 10(1), pp.13-26.
- Shen, W. and Ginis, I., 2003. Effects of surface heat flux-induced sea surface temperature changes on tropical cyclone intensity. *Geophysical research letters*, 30(18).
- Sikirić, M.D., Janeković, I. and Kuzmić, M., 2009. A new approach to bathymetry smoothing in sigma-coordinate ocean models. *Ocean Modelling*, 29(2), pp.128-136.
- Taylor, P.K. and Yelland, M.J., 2001. The dependence of sea surface roughness on the height and steepness of the waves. *Journal of physical oceanography*, 31(2), pp.572-590.
- Wallemacq, P. et al., 2018. Economic losses, poverty & disasters: 1998-2017. Centre for Research on the Epidemiology of Disasters, CRED. https://www.preventionweb.net/files/61119_credeconomiclosses.pdf

- Wang, H., M. Xu, A. Onyejuruwa, Y. Wang, S. Wen, A. E. Gao, Y. Li. Tropical Cyclone Damages in Mainland China over 2005-2016: Losses Analysis and Implications. *Environment, Development and Sustainability*, 2019, 21, 3077–3092.
- Warner, J.C., C.R. Sherwood, H.G. Arango, and R.P. Signell, 2005a: Performance of four Turbulence Closure Methods Implemented using a Generic Length Scale Method. *Ocean Modelling*, 8, 81-113.
- Warner, J.C., Armstrong, B., He, R. and Zambon, J.B., 2010. Development of a coupled ocean–atmosphere–wave–sediment transport (COAWST) modeling system. *Ocean modelling*, 35(3), pp.230-244.
- Wilkin, J.L., H.G. Arango, D.B. Haidvogel, C.S. Lichtenwalner, S.M. Durski, and K.S. Hedstrom, 2005: A regional Ocean Modeling System for the Long-term Ecosystem Observatory. *J. Geophys. Res.*, 110, C06S91, doi:10.1029/2003JC002218.
- Xu, Y., He, H., Song, J., Hou, Y. and Li, F., 2017. Observations and modeling of typhoon waves in the South China Sea. *Journal of Physical Oceanography*, 47(6), pp.1307-1324.
- Yablonsky, R.M. and Ginis, I., 2009. Limitation of one-dimensional ocean models for coupled hurricane–ocean model forecasts. *Monthly Weather Review*, 137(12), pp.4410-4419.
- Yamaguchi, M., Ishida, J., Sato, H. and Nakagawa, M., 2017. WGNE intercomparison of tropical cyclone forecasts by operational NWP models: A quarter century and beyond. *Bulletin of the American Meteorological Society*, 98(11), pp.2337-2349.
- Young, I.R. and Burchell, G.P., 1996. Hurricane generated waves as observed by satellite. *Ocean Engineering*, 23(8), pp.761-776.
- Zambon, J.B., He, R. and Warner, J.C., 2014a. Investigation of hurricane Ivan using the coupled ocean–atmosphere–wave–sediment transport (COAWST) model. *Ocean Dynamics*, 64(11), pp.1535-1554.
- Zambon, J.B., He, R. and Warner, J.C., 2014b. Tropical to extratropical: Marine environmental changes associated with Superstorm Sandy prior to its land-fall. *Geophysical Research Letters*, 41(24), pp.8935-8943.
- Zhang, F., Weng, Y., Gamache, J.F. and Marks, F.D., 2011. Performance of convection-permitting hurricane initialization and prediction during 2008–2010 with ensemble data assimilation of inner-core airborne Doppler radar observations. *Geophysical Research Letters*, 38(15).
- Zhao, X. and Chan, J.C., 2017. Changes in tropical cyclone intensity with translation speed and mixed-layer depth: idealized WRF-ROMS coupled model simulations. *Quarterly Journal of the Royal Meteorological Society*, 143(702), pp.152-163.

Table 1 Summary of configurations across the three component models

	WRF	ROMS	SWAN
Domain	D01: 400x400 (9km) D02: 400x400 (3km) 50 sigma-P hybrid vertical layers (ECMWF L50)	D01: 900x600 (2.2km) 30 sigma layers (12 layers in the upper 200m)	D01: 900x600 (2.2 km)
Initial and Boundary Conditions	ERA5 0.25° Hourly reanalysis 24-hr spin-up (FNL 0.25° vortex initial + grid nudging), warm restart	/12° HYCOM reanalysis Open boundary: N/E/S; Closed boundary: W LP optimized bathymetry: 10m-3000m Tidal forcing turned off	NOAA Wave Watch III 30 arc-minute hindcast data
Dynamics	dt=30 s D01 Spectral nudging, XY_NWave=4 (900km, 400hPa and upper)	dt=5 s Maximum current speed limit: 100m/s	dt=180 s Direction: 10°/bin (36 bins) Frequency: 0.04Hz–1Hz, 1s/bin (24 bins)

	WRF	ROMS	SWAN
Physics	mp_physics: Morrison double-moment ra_lw_physics: RRTMG ra_sw_physics: RRTMG sf_surface_physics: unified Noah land-surface model bl_pbl_physics: MYJ TKE scheme (WRF-SWAN) cu_physics: Grell-3 scheme (D01), turned off (D02)	Vertical Mixing: GLS_MIXING (Warner et al. 2005) Stability Function: Kantha and Clayson (1994)	Whitecapping: Komen et al. (1984) Breaking: Turned on (Cb=0.73) Bottom Friction: Madsen et al. (1988) Surface Roughness: C2008 (high-wind-and- young-sea) & TY2001 (normal run)
Global Settings	Coupling frequency: 1800s, all components initiated at 12Z September 13, 2018 and spin-up for 24 hours		

Table 2 Experimental Design

Experiment	Active Components	Wave-Air Roughness Scheme
TY2001	WRF+ROMS+SWAN (AWO)	Taylor and Yelland (2001)
C2008	WRF+ROMS+SWAN (AWO)	Caulliez et al. (2008)
WRFROMS	WRF+ROMS (AO)	N/A
WRFONLY	WRF (A)	N/A

Table 3 Root-mean-square error for crucial variables

Variable	QF303	QF306	QF307	Mean
Experiment				
Wind Speed (m s⁻¹)				

Variable	QF303	QF306	QF307	Mean
Experiment				
C2008				
TY2001				
WRFROMS				
WRFONLY				
Surface				
Pressure				
(hPa)				
C2008				
TY2001				
WRFROMS				
WRFONLY				
Sea Surface				
Tempera-				
ture				
(K)				
C2008				
TY2001				
WRFROMS				
Significant				
Wave				
Height (m)				
C2008				
TY2001				